Correspondence to:
S. Gruber,
simon.gruber@kit.edu

A Process Study on Thinning of Arctic Winter Cirrus Clouds With High-Resolution ICON-ART Simulations

Simon Gruber[1] , Ulrich Blahak[2], Florian Haenel[1], Christoph Kottmeier[1], Thomas Leisner[1], Harel Muskatel[3], Trude Storelvmo[4] , and Bernhard Vogel[1]

[1]Institute of Meteorology and Climate Research, Karlsruhe Institute of Technology, Karlsruhe, Germany, [2]German Weather Service, Offenbach, Germany, [3]Israel Meteorological Service, Bet-Dagan, Israel, [4]Department of Geosciences, University of Oslo, Oslo, Norway

Abstract In this study, cloud-resolving simulations of a case study for a limited area of the hibernal Arctic were performed with the atmospheric modeling system ICON-ART (ICOsahedral Nonhydrostatic-Aerosol and Reactive Trace gases). A thorough comparison with data both from satellite as well as aircraft measurement is presented to validate the simulations. In addition, the model is applied to clarify the microphysical processes occurring when introducing artificial aerosol particles into the upper troposphere with the aim of modifying cirrus clouds in the framework of climate engineering. Former modeling studies investigating the climate effect of this method were performed with simplifying assumptions and much coarser resolution, reaching partly contradicting conclusions concerning the method's effectiveness. The primary effect of seeding is found to be a reduction of ice crystal number concentrations in cirrus clouds, leading to increased outgoing longwave radiative fluxes at the top of the atmosphere, thereby creating a cooling effect. Furthermore, a secondary effect is found, as ice crystals formed from the injected seeding aerosol particles lead to enhanced riming of cloud droplets within the planetary boundary layer. This effectively reduces the coverage of mixed-phase clouds, thus generating additional cooling by increased upward longwave radiative fluxes at the surface. The efficacy of seeding cirrus clouds proves to be relatively independent from the atmospheric background conditions, scales with the number concentrations of seeding particles, and is highest for large aerosol particles.

1. Introduction

Being confronted with climate change due to anthropogenic emission of greenhouse gases, concerned climate scientists have proposed several ideas on how to compensate or at least decelerate climate warming (Caldeira et al., 2013; Crutzen, 2006). The methods in the framework of so-called climate engineering can generally be divided into two types. Carbon dioxide (CO_2) removal techniques aim at an active reduction of CO_2 in the atmosphere (Caldeira et al., 2013). The goal of other methods is to modify the Earth's radiation budget by solar radiation management.

As clouds exert a strong influence on the Earths' energy balance (Wild et al., 2015), several methods were proposed that focus on large-scale modification of clouds to achieve surface cooling, for example, increasing the albedo and thus the reflectivity of low-level marine stratocumulus clouds by injecting hygroscopic aerosol into pristine regions (Latham, 1990, 2002). Another idea enjoying growing attention was proposed by Mitchell and Finnegan (2009). Here, the outgoing longwave radiation (OLR) emitted from the Earth and the atmosphere is to be enhanced by thinning or even removing cirrus clouds in the upper troposphere.

Cirrus clouds are characterized by the absence of liquid droplets and are found at high altitudes and temperatures below 235 K (Pruppacher & Klett, 1997). Covering between 17% (Sassen et al., 2008) and 30% (Rossow & Schiffer, 1999) of the upper troposphere, they play a decisive role for both the water vapor budget of the upper troposphere and the Earth's energy budget (Myhre et al., 2013). Their net warming effect has been confirmed by analyzing satellite data (Chen et al., 2000; Futyan et al., 2005; Hartmann et al., 1992; Hong et al., 2016; Matus & L'Ecuyer, 2017), in situ observations (Kienast-Sjögren et al., 2016), and modeling studies (Gasparini & Lohmann, 2016).

Two contributions lead to this effect: As cirrus clouds reflect incoming solar shortwave radiation, they cause a certain cooling. By absorbing longwave (LW) radiation from warm sources like the Earth's surface and

Resources: Simon Gruber, Ulrich Blahak, Christoph Kottmeier, Harel Muskatel
Supervision: Ulrich Blahak, Christoph Kottmeier
Visualization: Simon Gruber, Ulrich Blahak
Writing - review & editing: Simon Gruber, Ulrich Blahak

the atmosphere beneath them, and emitting to space at much lower temperatures, a net warming effect results at the top of the atmosphere (TOA). As the LW warming effect outweighs the shortwave cooling, a net warming of 5 to 6 W/m^2 results (Gasparini & Lohmann, 2016; Hong et al., 2016). Therefore, a reduction or even removal of cirrus clouds would result in a cooling effect. However, the radiative effects of cirrus clouds crucially depend on their optical depth and altitude, cloud microphysical parameters like ice crystal number concentration, size, and shape, as well as on surface temperature and reflectivity (Corti & Peter, 2009; Fusina et al., 2007; Joos et al., 2014).

Ice crystals in cirrus clouds can form by different processes. Spontaneous freezing of supercooled liquid aerosol particles, such as sulfuric acid and sulfate solution, is called homogeneous nucleation. Besides the ubiquitous solution droplets, this process requires temperatures below approximately 235 K and supersaturation above approximately 145% (Kärcher & Lohmann, 2002). Homogeneous nucleation occurs in a "burst", once these requirements are fulfilled (Barahona & Nenes, 2009a). Depending on temperature, vertical velocity, droplet volume, and vapor pressure (Koop et al., 2000), up to several thousands of small ice crystals (1 to 10 μm) are formed (Krämer et al., 2016). Due to the resulting high ice crystal number concentrations (n_{ICE}), crystals will stay small, as the consumption of water vapor during nucleation limits their growth (Ickes et al., 2015).

Another process that leads to formation of ice crystals is heterogeneous ice nucleation on suitable ice-nucleating particles (INP). This process is not fully understood yet, but there is robust evidence that the ice-nucleating efficiency is dependent on particle size and chemistry (Hoose & Möhler, 2012). Most effective are insoluble aerosol particles such as mineral dust, metallic particles, several types of biological particles, and possibly also soot (Phillips et al., 2008). The ice nucleation efficiency of particles is determined on a molecular level by local surface features acting as active sites aiding ice growth (Kiselev et al., 2017).

Heterogeneous ice nucleation requires lower supersaturation and can occur at higher temperatures than homogeneous nucleation, as the INP facilitate the phase transition necessary by lowering the energy barrier of freezing (Hoose & Möhler, 2012; Kärcher & Lohmann, 2003). In the upper troposphere, INP occur in much smaller number concentrations than the ubiquitous solution droplets, usually not exceeding 10 L^{-1} (DeMott et al., 2003). Therefore, fewer ice crystals result from heterogeneous than from homogeneous ice nucleation and in the former case, ice crystals can grow to larger sizes of tens of micrometer (Barahona & Nenes, 2009a; Kärcher et al., 2006; Kuebbeler et al., 2014). Although INP seem to occur only sparsely, they can have a large impact on cloud formation (Gettelman et al., 2012), as both nucleation mechanisms compete for the available water vapor (Lohmann et al., 2008). With suitable low supersaturation and vertical velocity, ice crystals formed by heterogeneous nucleation can, by depleting excess water vapor, compensate for the increase of supersaturation due to updrafts and even reduce supersaturation. Thereby, homogeneous nucleation can be suppressed or even inhibited (DeMott et al., 1994).

Based on the debatable (Cziczo et al., 2013) assumption that homogeneous nucleation is the dominant formation process of cirrus clouds, the idea of Mitchell and Finnegan (2009) makes use of the competition between the two nucleation mechanisms. Artificially injected INP in suitable regions could trigger heterogeneous ice nucleation and suppress homogeneous nucleation. Compared to ice crystals in natural cirrus clouds, the ice crystals would in that case occur in much lower number concentrations. As they would also be larger and grow even further, sedimentation would remove them efficiently from the high altitudes, thus reducing cirrus lifetime. In addition, their optical depth would be reduced (Jensen et al., 2016; Kärcher & Ström, 2003). Both would result in a smaller warming effect. Furthermore, sedimenting ice crystals effectively removes water vapor that is among the most important greenhouse gases.

Several studies using global climate models (GCM) on climatic temporal scales investigated this method with partly contradicting results concerning the method's effectiveness. Hypothetically, removing all cirrus clouds from the atmosphere could compensate more than the effect of CO$_2$ doubling, resulting in a net cooling effect of 5 to 6 W/m^2 (Gasparini & Lohmann, 2016; Hong et al., 2016). However, the difference between scenarios where all cirrus clouds originate from either pure homogeneous or pure heterogeneous nucleation, respectively, is about 2 to 3 W/m^2 and thus compensates for at least 50% to 80% of a CO$_2$ doubling (Lohmann et al., 2008; Storelvmo et al., 2013). Assuming a background where 50% of all mineral dust acts as INP, Storelvmo and Herger (2014) introduced artificial INP becoming active at 105% supersaturation. Limiting the seeding to regions with temperatures lower than 235 K results in a significant negative effective radiative forcing with a maximum value of −2 W/m^2 when seeding with 18 particles per liter. Global

average surface air temperatures were reduced by 1.4 K. Limiting the seeding to winter polar regions, and thereby impact only 15% of the Earth, turns out to be sufficient; as here, due to generally low natural aerosol loading in the upper troposphere (Kärcher & Lohmann, 2003), homogeneous nucleation might be dominant (Storelvmo & Herger, 2014).In addition, due to reduced or lacking solar radiation caused by low solar angles during polar night, the net radiation effect is maximized (Storelvmo et al., 2014). In addition, possible self-enhancing feedback mechanism due to restoring Arctic sea ice cover might further increase the efficacy of the method.

However, Penner et al. (2015) found only about -0.33 ± 0.21 W/m^2 with seeding concentrations of 20 L^{-1}. They attribute the large differences compared to former studies to different assumptions made. In their simulations, secondary organic aerosol acts as INP subgrid scale updraft velocity is not limited. Likewise, Gasparini and Lohmann (2016) do not find a significant cooling effect due to seeding. In that study, in contrast to others, ice crystal sizes decrease with seeding. This effect more than outweighs the reduction in n_{ICE}. They conclude that ice crystals formed by seeding consume enough excess water vapor to cause decreasing sizes of the remaining crystals. In addition, seeding leads to artificial cirrus cloud formation in supersaturated but cloud-free regions. This effect gains importance, when extraordinarily effective INP are used.

Another type of studies used a prescribed increased sedimentation velocity of ice crystals as proxy for seeding (Crook et al., 2015; Jackson et al., 2016; Muri et al., 2014). This approach can reproduce surface climate responses to seeding but is unable to capture the changes in cloud microphysical processes that occur when considering seeding aerosol in a cirrus formation parameterization (Gasparini et al., 2017). Applying the latter approach, a large fraction of the seeding effect is outweighed by a reduction in liquid clouds in response to increased convective activity. In addition, redistribution of ice to lower levels leads to glaciation and consequential reduction of mixed-phase clouds causing a warming effect.

Besides searching for configurations that achieve the strongest cooling, it is of at least equal importance to emphasize possible undesirable side effects of seeding cirrus clouds. If too many seeding aerosol particles are injected, cirrus clouds get optically thicker than natural ones, leading to a warming effect (Storelvmo & Herger, 2014). The same occurs when the seeding INP are present in regions dominated by heterogeneous ice nucleation, and they cannot reduce supersaturation enough to prevent nucleation on natural INP (Kärcher et al., 2006). A crucial assumption within all of the approaches mentioned is the fraction of homogeneous and heterogeneous nucleation in the unseeded atmosphere. Several studies point at homogeneous nucleation being the dominant process in cirrus formation (Mitchell et al., 2011; Spichtinger et al., 2003, 2004). However, in situ measurements indicate that, at least over certain regions, n_{ICE} is lower than expected from homogeneous nucleation, indicating that heterogeneous ice nucleation is the main freezing mechanism (Cziczo et al., 2013; Jensen et al., 2013; Krämer et al., 2016).

The studies mentioned above exclusively used GCMs to investigate the effects of seeding. As vertical wind velocity (w) determines supersaturation, a realistic distribution of w is crucial for obtaining realistic fractions of heterogeneous and homogeneous nucleation (Pruppacher & Klett, 1997). However, due to the coarse resolution in most GCMs, w remains a large source of uncertainty.

Cirrus seeding in former studies was performed in a straightforward manner, by either prescribing an increased sedimentation as proxy (e.g., Muri et al., 2014) or assuming a "perfect" seeding scenario with regard to the ice nucleation properties of the INP, the concentrations, and the injection into altitudes most susceptible for seeding (e.g., Gasparini et al., 2017; Storelvmo et al., 2013).

This study aims at getting detailed insight into the cloud microphysical processes affected by more realistic seeding scenarios using the temporal and spatial high-resolution modeling system ICON (ICOsahedral Nonhydrostatic)-ART (Aerosol and Reactive Trace gases; Rieger et al., 2015; Zängl et al., 2015) coupled with a sophisticated two-moment cloud microphysical scheme (Seifert & Beheng, 2006).

The effects of seeding aerosol with nucleating properties like mineral dust injected in various scenarios into the atmosphere are explored. Furthermore, due to the high resolution, the impact of cirrus seeding on lower-lying mixed-phase clouds can be investigated, as the effect of seeding here has been proposed to outweigh much of the desired outcome (Gasparini et al., 2017).

As several studies find seeding being most effective in polar winter conditions, the focus is on a period of the Arctic winter 2015/2016. During this time, the combined Polar Stratosphere in a Changing Climate
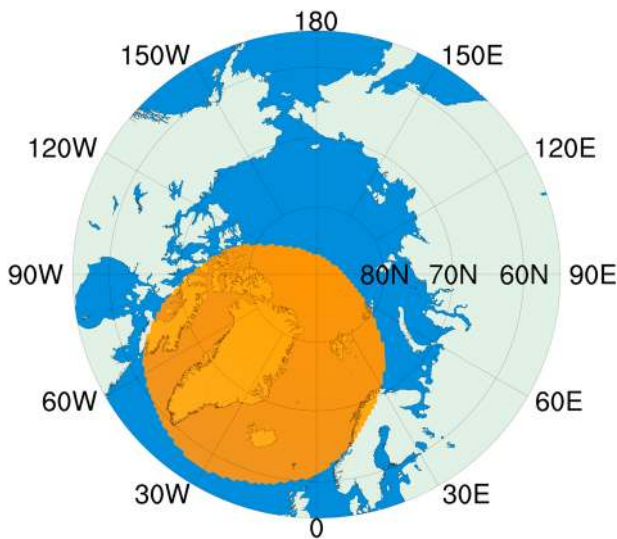
Figure 1. Simulation domain for this study.

(https://www.polstracc.kit.edu)/GW-LCYCLE II (Investigation of the life cycle of gravity waves; http://www.pa.op.dlr.de/gwlcycle2/) / SALSA (Seasonality of Air mass transport and origin in the Lowermost Stratosphere using the HALO [High Altitude and Long Range Research Aircraft] Aircraft) campaign, in the following abbreviated by "PGS," took place and is one of the rare hibernal Arctic airborne field campaigns in the recent past.

2. Methods

The online coupled modeling system ICON-ART is used. ICON consists of a nonhydrostatic dynamical core and packages of physical parameterizations suitable for numerical weather prediction, climate modeling, and large eddy simulations (Heinze et al., 2017; Zängl et al., 2015).

The ART module is able to simulate the evolution of atmospheric trace gases and aerosol species and the associated impacts on both cloud microphysics and radiative fluxes (Rieger et al., 2015). A description of the decisive parts of the model is deferred in the appendix.

Here, the model is operated in a so-called limited area mode. Unlike global modeling systems, only a certain area is selected as simulation domain, and lateral boundary conditions for meteorological variables are updated hourly. This allows the conduction of a large number of computational relatively inexpensive simulations with high spatial and temporal resolution.

However, it is crucial to note that as no two-moment cloud microphysics are applied in the models providing the driving data, no hydrometeor number concentrations are passed when updating the boundaries. Instead, they are determined by dividing mass concentrations by a fixed mean mass of a single hydrometeor.

The spatial resolution is R2B09, corresponding to an effective horizontal mesh size of approximately 5 km and 50 vertical levels reaching up to 20 km hence resulting in a mean distance between the model layers of ~1,000 m in the upper troposphere and ~10 m close to the surface. The integration time step is 25 s, and convection is calculated explicitly by the model, that is, no convection scheme is applied.

Choosing a convection-permitting resolution has several benefits. First, a more realistic distribution of vertical velocity is obtained, as the latter strongly depends on horizontal resolution (Rauscher et al., 2016). As discussed in the previous section, updraft speeds crucially determine the competition between homogeneous and heterogeneous nucleation (Barahona et al., 2017). Furthermore, a high resolution allows explicit simulation of a larger fraction of clouds, in contrast to GCMs with coarse resolutions.

3. Case Study

In contrast to earlier modeling studies investigating the impact of seeding aerosol on cirrus clouds, the present study makes use of an entirely different model setup. Due to the high spatial and temporal resolution, a thorough comparison of the simulated atmospheric processes with measurement data is possible. Besides, the present study is one of the few attempts yet of high-resolution modeling of Arctic cirrus clouds. The following analyses are based on a case study. As mentioned before, polar regions are thought to be the most susceptible regions for seeding cirrus clouds due to their low natural aerosol loading, although these findings are still afflicted with uncertainties (Glantz et al., 2014; Xie et al., 2018), and the absence of solar radiation during polar night. Furthermore, the possible feedback mechanisms might be able to, at least partly, restore sea ice cover and hence increase the overall efficacy of the method (Storelvmo et al., 2014). Therefore, the focus is on a limited area including Greenland and parts of the Arctic basin and the Norwegian Sea (Figure 1). This region downstream of Greenland can be affected by the formation of orographically induced cirrus clouds (Kärcher & Ström, 2003). The case covers a single day during Arctic winter (20 January 2016), as on this day, measurement flights connected to the PGS campaign took place over the region, facilitating validation of the simulations.

3.1. Natural Aerosol

In this study, time constant, horizontally homogeneous profiles for the three modes (see Table A1) of mineral dust and sea salt aerosol are prescribed, obtained from a 2-week spin-up simulation with ICON-ART
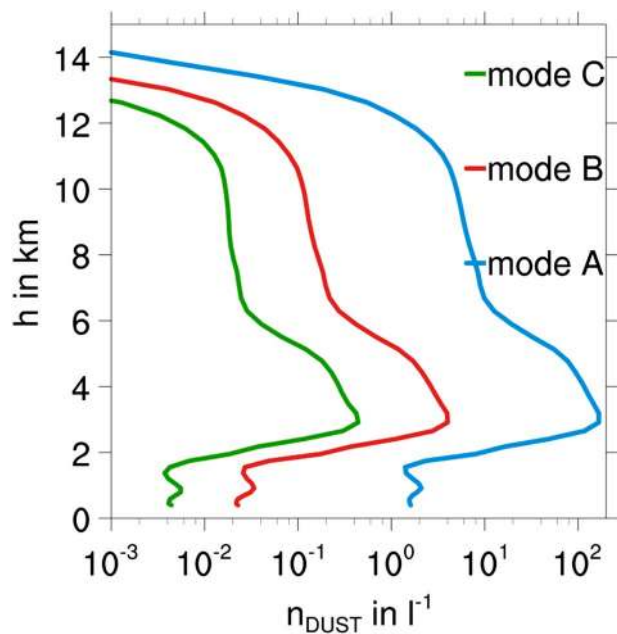
Figure 2. Averaged height profiles of number concentrations (n_{DUST}) for the three modes of mineral dust.

covering the entire globe. Mineral dust over the Arctic (Figure 2) originates from sources far away from the simulation domain, mainly located in the Sahara. Due to the long-range transport, number concentrations are generally low. At altitudes between 8 and 13 km, where cirrus formation is expected, henceforth thus termed as the "cirrus region," number concentrations of mineral dust (n_{DUST}) for mode A do not exceed 1 to 10 L^{-1}. Such values agree with those reported in other studies (e.g., Cziczo et al., 2013). Within the well-mixed planetary boundary layer (PBL), mineral dust that sedimented from above experiences strong dilution, resulting in low average values of n_{DUST} for mode A around 1–2 L^{-1}.

The highest values for n_{DUST} are located just above the PBL between 2 and 5 km above ground, reaching approximately 120 L^{-1} for the smallest mode A (Table A1) and decaying strongly with height beyond. Prior to the date considered for this study, a special synoptic situation led to an unusual, intense warming of the Arctic region north of Europe. Subtropical air was transported poleward due to an intense low-level jet and reached the area north of Svalbard within the outflow of a warm conveyor belt (Binder et al., 2017). Due to low temperatures at the ground of the region forming a layer of cold air, the dust-laden, warmer air masses were forced to rise, causing the maximum mineral dust concentrations at altitudes between 2 and 5 km.

As mean dust aerosol diameters do not change much with height, values constant with height for each mode are prescribed according to Table A1.

In order to gain more confidence about the mineral dust concentrations used, simulations are carried out varying the profiles for the three modes by orders of magnitude according to Table 1. For a first comparison, data gathered from the CALIPSO (Cloud-Aerosol Lidar and Infrared Pathfinder Satellite Observations) satellite (Winker et al., 2007, 2009) is used. The satellite is one component of the A-train satellite constellation (Stephens et al., 2002). With an orbit inclination of 98.2°, daily measurements over the polar regions up to 82°N are available. Aboard the satellite, the Cloud-Aerosol Lidar with Orthogonal Polarization instrument (Hunt et al., 2009; Powell et al., 2009) is mounted, measuring backscatter at wavelengths of 1.064 and 0.532 μm, respectively; thus, as not reliant upon solar radiation, it is able to gain data also during polar night. In the following, the data analyzed are based on the retrieval for the extinction coefficient at 0.532 μm from v3 Cloud-Aerosol Lidar with Orthogonal Polarization Level 2 Profile Cloud product available through the NASA Langley Atmospheric Science Data Center (http://eosweb.larc.nasa.gov) with a horizontal resolution of 5 km.

In Figure 3, a comparison of the CALIPSO extinction coefficient retrieval for ice clouds only and the simulations listed in Table 1 is done. The simulated extinction coefficient for the nearest wavelength band (0.550 μm), calculated as described in section C, is used, that is, no instrument simulator or forward operator is applied. Values of the grid cells nearest to the geolocations of the CALIPSO retrieval are compared and sampled for all swaths of CALIPSO during the 24-hr integration time of the simulations.

Throughout the chosen codomain of both temperature and extinction coefficient, all simulations and the observation agree reasonably well within the temperature range between 225 and 255 K. However, as indicated by the contour in Figure 3b, *HET1* overestimates the frequency of occurrence of extinction coefficients larger than 1 km^{-1} at temperatures below 225 K, that is, at higher altitudes. This hints at cirrus clouds in the simulation being too optically tick, caused be either overestimated ice water content (IWC) or too small ice crystals and overestimated values for n_{ICE}. The latter may be caused by homogeneous nucleation being too dominant. Prescribing strongly enhanced number concentrations of mineral dust, as in simulations *HET100* and *HET1000* leads to suppression of homogeneous nucleation and hence results in fewer but larger ice crystals and reduced optical thickness.

At temperatures above 260 K, the extinction coefficient is strongly underestimated, that is, the model underestimates both IWC and n_{ICE}. Here, enhanced values for n_{DUST} do not reduce the deviations. This may at least partly attributed to the absence of other possible INP except mineral dust in the simulations. Throughout
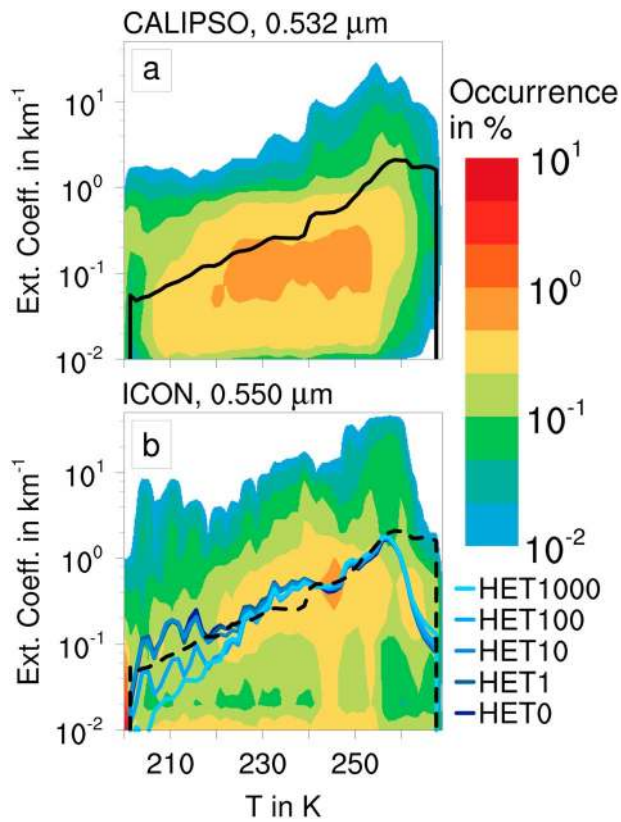
Figure 3. Two-dimensional probability distribution of the extinction coefficient with respect to temperature sampled along all tracks of CALIPSO crossing the simulation domain during the entire integration time for (a) CALIPSO and (b) simulation *HET1* (Table 1). The median extinction coefficients in each temperature bin are indicated by lines: black solid in (a) and dashed in (b). CALIPSO; colors in (b): simulations according to Table 1. CALIPSO = Cloud-Aerosol Lidar and Infrared Pathfinder Satellite Observations; ICON = ICOsahedral Nonhydrostatic.

the further analyses, HET1, that is, prescribing mineral dust according to Figure 2 without a scaling factor will be considered as the reference (*REF*). However, it is important to note that due to lack of measurements, there is large uncertainty concerning these values. Therefore, the fraction of homogeneously nucleated ice crystal and n_{ICE} may be overestimated in this study.

3.2. Supersaturation

Focusing on the hibernal Arctic makes model validation a challenging task. Most satellite sensors are unable to gather data in the absence of solar radiation during polar night, and in situ measurement campaigns usually are not conducted in winter, presumable by virtue of similar reasons. Providentially, during the PGS campaign, both in situ and remote sensing data were gathered on numerous flights of the two DLR (Deutsches Zentrum für Luft- und Raumfahrt) research aircraft HALO and Falcon. Among other objectives, the campaign aimed at investigating the structure and composition of the Arctic upper troposphere and lower stratosphere, chemical and physical processes leading to Arctic stratospheric ozone depletion, and transport and mixing processes in the upper troposphere and lower stratosphere (UTLS) at high latitudes (e.g., Khosrawi et al., 2017). In the following, analyses are performed for 20 January 2016, the day on which PGS flight 8 was carried out.

The very basis of ice crystal nucleation is water vapor supersaturation with respect to ice. To simulate realistic cloud formation, a crucial requirement for atmospheric models is therefore that they generate realistic distributions of humidity. However, also in this context, model validation is challenging. While there are in situ measurements of humidity in the UTLS region with high time resolution and accuracy available (e.g., Krämer et al., 2009), they are limited to the flight tracks of their carriers. In contrast, data obtained from large-scale satellite observations suffer from a limited vertical resolution (Lamquin et al., 2012).

During PGS, HALO was equipped with the GLORIA (Gimballed Limb Observer for Radiance Imaging of the Atmosphere) instrument. GLORIA is a limb-imaging Fourier transform spectrometer with its line of sight penetrating horizontally the Earth's atmosphere tangential to the Earth's surface. It is a remote sensing instrument, especially designed to measure vertical profiles of trace gases like water vapor with high accuracy and with a high spatial resolution in the UTLS. Details about GLORIA are discussed by Friedl-Vallon et al. (2014) and Riese et al. (2014). For the comparison in this study, the cloud index (Spang et al., 2004) and retrievals of water vapor (H_2O) and temperature based on "chemistry" mode measurements are used.

The cloud index (Spang et al., 2004) is a spectral color ratio applied to infrared limb observations and is sensitive to increasing opacity in the presence of clouds. Usually, cloud index values close to 1 indicate opaque conditions due to optically dense clouds, while cloud index values above 4 indicate cloud-free conditions. Values in between indicate partly cloud-affected conditions due to the presence of partly transparent clouds or measurements with the instrument's field of view covering clouds only partly. The GLORIA cloud index data for PGS08 show clearly distinguished cloud patterns below flight altitude and are therefore well suited for a qualitative comparison with ICON-ART with respect to the locations and extents of clouds.

The water vapor volume mixing ratio and temperature are retrieved from the GLORIA observations involving a radiative transfer model and inversion algorithm (Johansson et al., 2018, and references therein). Furthermore, relative humidity is calculated from the GLORIA temperature and water vapor data. With GLORIA measurements affected by opaque clouds, that is, cloud index close to 1, no atmospheric parameter retrieval is possible. Hence, gaps result in the GLORIA temperature, water vapor, and ice supersaturation data in the presence of clouds. Moderate vertical resolutions of typically 0.5 to 1 km were achieved for the retrieved profiles. Data points with vertical resolutions lower than 2.0 km are excluded here.

Table 1
Simulation Terminology and Characteristics

Simulation	$d_{0,\mathrm{SEED}}$ in micrometer	Seeding aerosol	Mineral dust
REF,	—	No	$\sqrt{}$
HET1			
HET0	—	No	No
HET10	—	No	$10 \times n_{\mathrm{DUST}}$
HET100	—	No	$10^2 \times n_{\mathrm{DUST}}$
HET1000	—	No	$10^3 \times n_{\mathrm{DUST}}$
SEED,	6.7	$\sqrt{}$	$\sqrt{}$
DIA6.7,			
SEED HET1			
TRGT	6.7	Only where hom. nuc. can be suppressed	$\sqrt{}$
TRGT2	6.7	Only where $T < 235$ K	$\sqrt{}$
DIA0.5	0.5	$\sqrt{}$	$\sqrt{}$
DIA1.5	1.5	$\sqrt{}$	$\sqrt{}$
DIA14.2	14.2	$\sqrt{}$	$\sqrt{}$
SEED HET0	6.7	$\sqrt{}$	no
SEED HET10	6.7	$\sqrt{}$	$10 \times n_{\mathrm{DUST}}$
SEED HET100	6.7	$\sqrt{}$	$10^2 \times n_{\mathrm{DUST}}$
SEED HET1000	6.7	$\sqrt{}$	$10^3 \times n_{\mathrm{DUST}}$

Note. Mineral dust concentrations for all simulations are prescribed according to the profiles depicted in Figure 2; the seeding aerosol concentrations follow the profile shown in Figure 6, unless otherwise stated.

Figure 4a shows the GLORIA cloud index data for the selected flight section. Gaps in the data correspond with a flight section where GLORIA was operated in a different mode (about 17:00 to 18:15 UTC) and time intervals of calibration measurements. Figure 4b shows a cloud mask generated from the model data along the geolocations of the GLORIA data, including also data where gaps are present in the measurement. This comparison is limited and can only be qualitative, as GLORIA cloud index and the cloud mask of the model are physically different quantities. The GLORIA data show dense clouds, that is, cloud index close to 1, around 15:40 UTC and shortly after 16:30 UTC. An optically less dense cloud is visible close to 19:00 UTC. All three observed cloud systems are reproduced by the model; however, they appear slightly displaced horizontally. Differences in the locations and fine structures of the clouds are explained by the distinct dynamics inherent to the forecast.
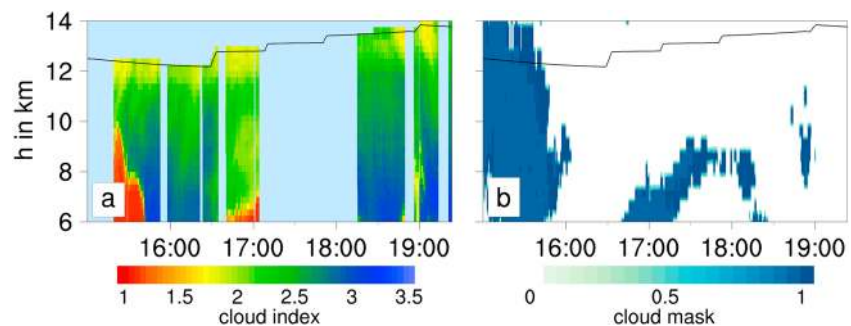

Figure 4. (a) Vertical cross section of cloud index derived from Gimballed Limb Observer for Radiance Imaging of the Atmosphere measurements during PGS08 on 20 January 2016. Low cloud index values indicate opaque conditions due to cloud particles along the instrument's line of sight. (b) Cloud mask derived from the model simulation at the geolocations of the measurement (0 = no cloud / 1 = cloud present). Black line in both panels: HALO flight altitude. Time is in universal time coordinated.
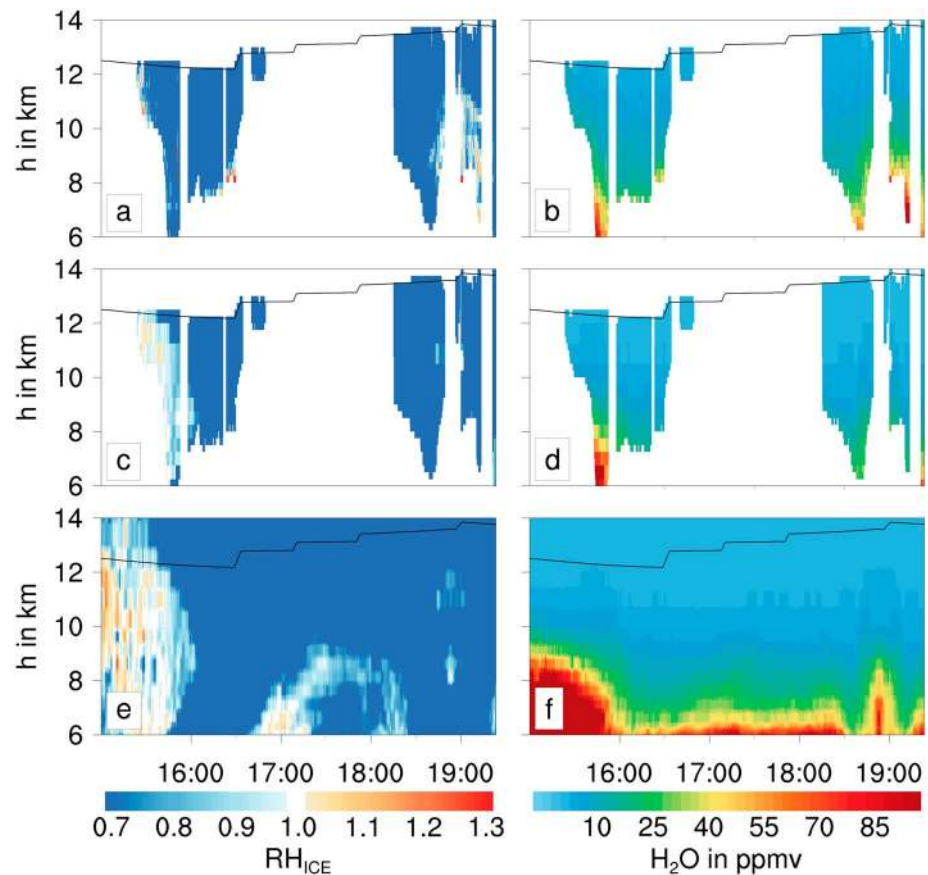
Figure 5. (a) Cross sections of relative humidity (i.e., supersaturation versus ice phase) and (b) water vapor volume mixing ratio derived from Gimballed Limb Observer for Radiance Imaging of the Atmosphere measurements during the HALO flight PGS08 on 20 January 2016. Relative humidity (c) and water vapor volume mixing ratio (d) simulated by the model and filtered for geolocations where Gimballed Limb Observer for Radiance Imaging of the Atmosphere data are available. Full vertical cross section of the same parameters from the model simulation (e, f). Time is in universal time coordinated.

Figure 5 shows GLORIA data of water vapor volume mixing ratio and relative humidity (i.e., ice supersaturation) together with the corresponding model data. The GLORIA and ICON-ART data consistently show typical stratospheric water vapor mixing ratios well below 10 ppmv around and above 10 km (Figure 5b and d/f). The observed absolute water vapor volume mixing ratios are reproduced very well by the model. In particular, the simulated increase of water vapor toward tropospheric values at altitudes below 9 km between 15:45 and 16:30 UTC and below 10 km after 18:15 UTC agrees very well with the observation.

The comparison of relative humidity derived from the GLORIA and model data is shown in Figures 5a and 5c/5e. Relative humidity well below 1 (blue) is consistently found in regions characterized by low stratospheric water vapor volume mixing ratios (Figures 5b and 5d/5f) and free of clouds (Figure 4). Both GLORIA and model data show enhanced relative humidity in the respective regions covered by clouds and their close vicinity. In context of the slightly different locations and patterns of cloud systems in observation and simulation, values of relative humidity simulated by the model match also very well with the GLORIA measurements. Therefore, the prerequisites for this model study are given.

4. Influence of Seeding

Various substances have been proposed to be used as INP for cirrus seeding. Ideally, the substance of choice should be very effective at nucleating ice at temperatures lower than $-20\,°C$ but ineffective at higher temperatures. Furthermore, it should be nontoxic and affordable. Several studies assumed seeding scenarios with such a perfect substance (e.g., Gasparini et al., 2017; Storelvmo et al., 2014), hence disregarding methods of deployment but rather assuming that the aerosol particles were in place in necessary concentrations.
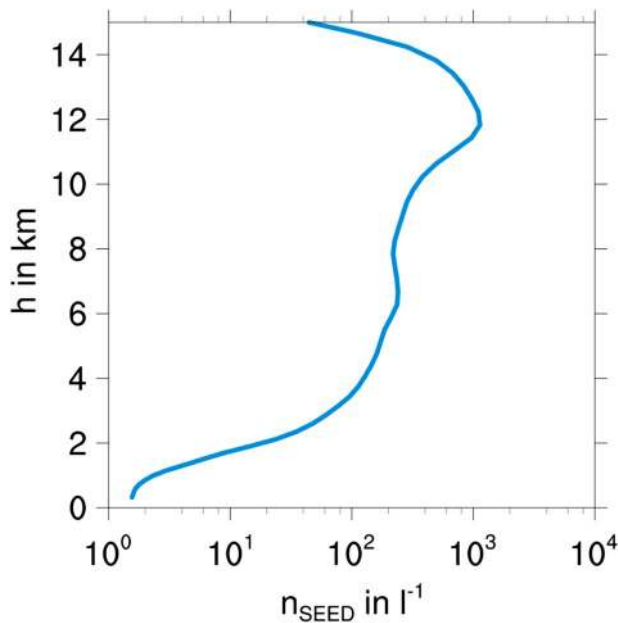
Figure 6. Averaged height profile of number concentrations for the seeding aerosol.

Suitable agents could be Bismuth tri-iodide (BiI_3; Mitchell & Finnegan, 2009) and mineral dust (Lohmann & Gasparini, 2017). However, not much is known about the ice nucleation properties of BiI_3 from laboratory studies or even field measurements, whereas mineral dust has been investigated to a much greater extent (e.g., Atkinson et al., 2013; Boose et al., 2016; Eastwood et al., 2008; Niemand et al., 2012). Therefore, in this study, the impact of a hypothetical deployment of seeding particles with ice-nucleating properties like mineral dust is examined.

Commercial aircraft could be a suitable means for delivery, being both affordable and already flying at the desired altitudes. Possible technical solutions could be either carrying the substance dissolved in the jet fuel and burn it to create the seeding aerosol or by injecting the substance into the engine exhaust forming the seeding aerosol in the jets' contrails (Mitchell & Finnegan, 2009). In this study, this idea of deployment is mimicked. To obtain an average height profile, a spin-up simulation of 2 weeks was performed, where deployment of the aerosol took place alongside aircraft trajectories at cruise altitude throughout the Northern Hemisphere. The trajectories were obtained using traffic way point information from Automatic Dependent Surveillance-Broadcast transponders on commercial airliners according to the method described in Gruber et al. (2018).

The average height profile of the seeding aerosol number concentrations (n_{SEED}) in the limited model area domain is depicted in Figure 6. Despite the absence of commercial flights over most parts of the Arctic region, the maximum concentration of seeding aerosol is located at the main cruise altitudes between 10 and 13 km. These high concentrations result from long-range transport, mostly due to the strong hibernal jet stream. Beneath, the concentrations drop about an order of magnitude, remaining largely at a constant value throughout the lower free troposphere. In the PBL, the aerosol is diluted due to turbulent processes and removed from the atmosphere by deposition and washout.

The scenarios evaluated in the following are summarized in Table 1. For all scenarios except REF, temporally constant and horizontally homogeneous seeding aerosol concentrations are prescribed following the profile shown in Figure 6. In contrast to former studies (e.g., Gasparini et al., 2017; Storelvmo & Herger, 2014), the seeding aerosol can also form ice at temperatures above 235 K. Hence, in addition to *SEED*, where seeding can possibly occur at all temperatures below freezing level, results of two highly idealized, more targeted strategies are examined. In *TRGT*, the same concentrations and aerosol sizes as in SEED are assumed to be in place only where homogeneous nucleation would occur, thus avoiding formation of artificial cirrus clouds in supersaturated but cloud-free regions and theoretically achieving the maximum possible elimination of cirrus clouds. Additionally, in *TRGT2*, seeding aerosol is only forming ice below temperatures of 235 K similar to the setup used in former studies. The discussion of the latter can be found in Appendix D.

4.1. Change in Nucleation Regimes

The averaged rate of heterogeneous nucleation occurring in areas with $T < 235$ K in REF is depicted in Figure 7a1. In the chosen temperature regime, homogeneous nucleation is possible and hence can be suppressed by heterogeneous nucleation on both natural and artificial INP indicated by ratios of heterogeneous to homogeneous nucleation rates close to unity. In REF, this occurs at the southern tip of Greenland, the northern parts of Canada, and in the region north of Scandinavia (Figure 7a3). Those areas are characterized by rather low average grid scale RH_{ICE} (Figure 8a) and updraft speeds (Figure 8b). In areas with either enhanced RH_{ICE} or strong updraft speeds, especially east of Greenland, homogeneous nucleation clearly dominates the formation of cirrus clouds (Figure 7a2).

Obviously, as heterogeneous nucleation is ubiquitous in the SEED scenario (Figure 7b1), homogeneous nucleation can be suppressed entirely throughout the domain (Figure 7b2), except for areas in the central and eastern Arctic. Apparently, even with seeding, either vertical velocity or supersaturation is large enough to still allow homogeneous nucleation to dominate in these regions. For the chosen situation, the large-scale flow crossing Greenland from southwest to northeast aids the formation of topography-induced lee waves
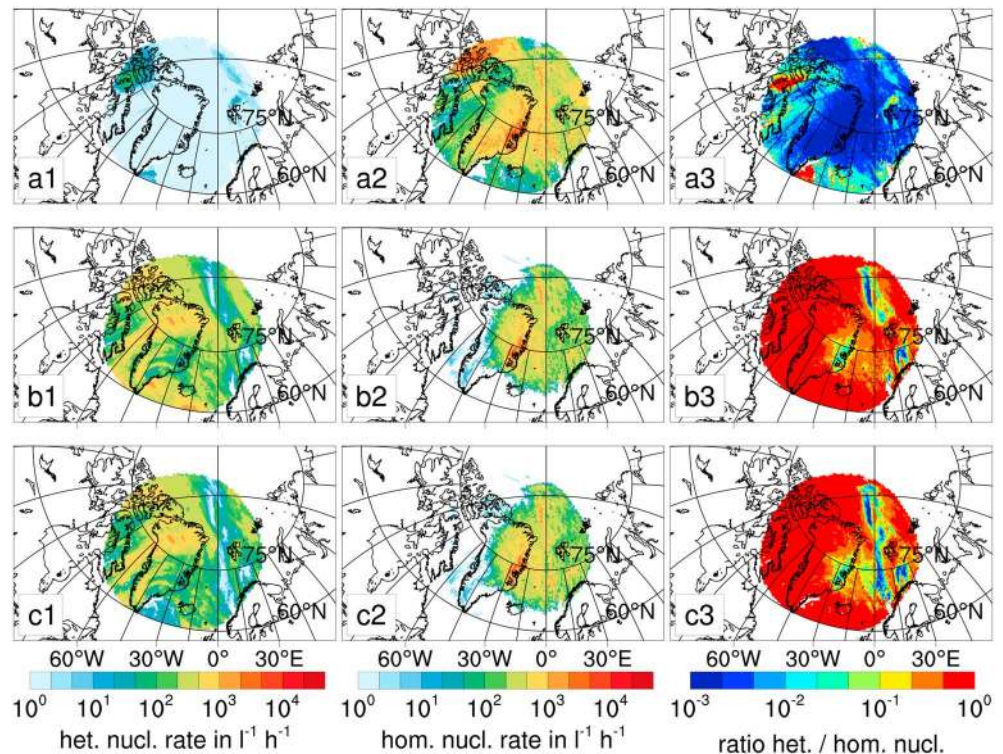
Figure 7. Heterogeneous (a1, b1, c1) and homogeneous nucleation rate (a2, b2, c2) and ratio of heterogeneous to homogeneous nucleation rates (a3, b3, c3) at $T < 235$ K for reference simulation (a1–a3), *SEED* (b1–b3), and *TRGT* (c1–c3) averaged over the entire domain and simulation time.

that in turn cause small-scale fluctuations in supersaturation, partly exceeding 2.0 (not shown). This in turn enhances homogeneous nucleation rates to such an extent that the present concentrations of seeding aerosol are too low to inhibit homogeneous nucleation. Nearly the same patterns can be found in TRGT, except for heterogeneous nucleation rates being lower over large parts of the domain, especially south of Greenland and the North Sea (Figure 7c1). In those regions, homogeneous nucleation rates are generally low in REF (Figure 7a2), that is, there is less need to suppress it.

4.2. Impact on Cirrus Clouds

The primary impact of seeding is the reduction of n_{ICE}, indicated in Figure 9a by large differences in column-integrated n_{ICE} for SEED and REF in regions with $T < 235$ K. Here, the concept of seeding cirrus clouds works as intended. However, only minor reductions or even an increase in column-integrated n_{ICE} occur south of Greenland and north of Svalbard, as those regions were dominated by heterogeneous nucleation already in REF (Figure 7a3). A moderate decrease in n_{ICE} occurs over northern Canada (Figure 9a), although heterogeneous nucleation partly is dominant in REF (Figure 7a3). However, the seeding effect still appears, as over this region, homogeneous nucleation rates are high (Figure 7a2).

In TRGT, the reduction in n_{ICE} is slightly enhanced (Figure 9b) compared to SEED. Also here, formation of artificial cirrus occurs, although to a weaker extent than with SEED. By construction, seeding aerosol act in this case as INP only where homogeneous nucleation can be suppressed. However, due to changes in cirrus cloud cover, relative humidity, and subsequent changes in stability and supersaturation downstream, the time, location, and frequency of occurrence of cirrus clouds can change in TRGT compared to REF.

A possibly undesirable effect of seeding is formation of artificial cirrus clouds in formerly supersaturated but cloud-free regions (Gasparini et al., 2017). This effect possibly can outweigh the reduction of n_{ICE} due to suppression of homogeneous nucleation. In SEED, a strong increase in n_{ICE} can be found in the temperature regime between 235 and 273 K (Figure 9c). As here, no homogeneous nucleation can happen and natural INP concentrations are generally low throughout the upper altitudes, injecting artificial INP has a strong impact. However, the column-integrated n_{ICE} also decreases on occasion due to enhanced upstream
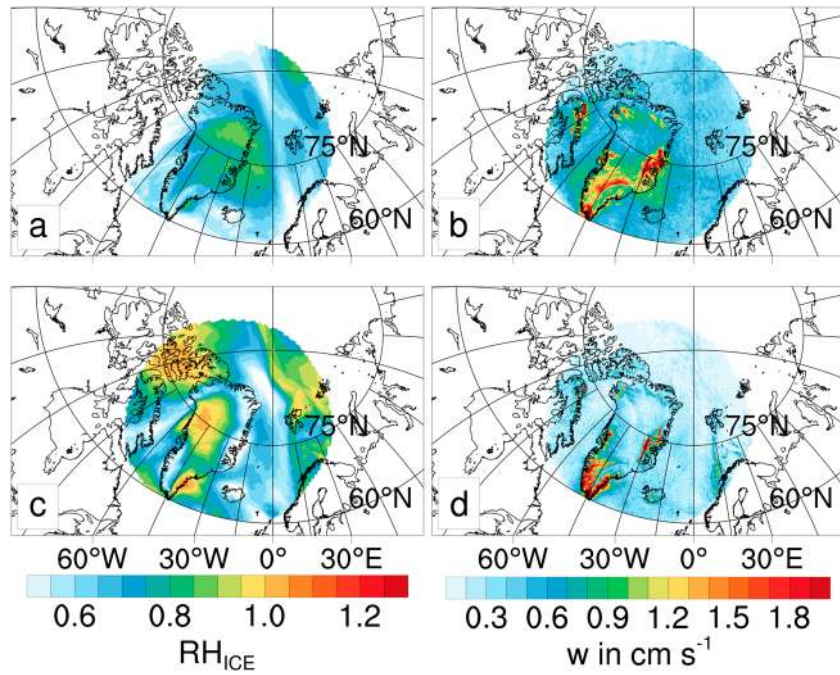
Figure 8. Relative humidity with respect to ice (a, c) and updraft speed (b, d) in *REF* in regions with $T < 235$ K (a, b) and $235K < T < 273$ K (c, d) averaged over the entire domain and simulation time.

consumption of excess water vapor by the ice crystals formed on the seeding aerosol. For the same reasons as discussed above, artificial cirrus also form in TRGT (Figure 9d) but to a smaller extent.

Vertical profiles of several cirrus properties averaged over the entire domain and simulation time are depicted in Figures 10a–10d. In Figure 10a, n_{LIM} is the minimum number concentration of ice crystals formed by heterogeneous nucleation in the reference simulation that still is able to inhibit homogeneous
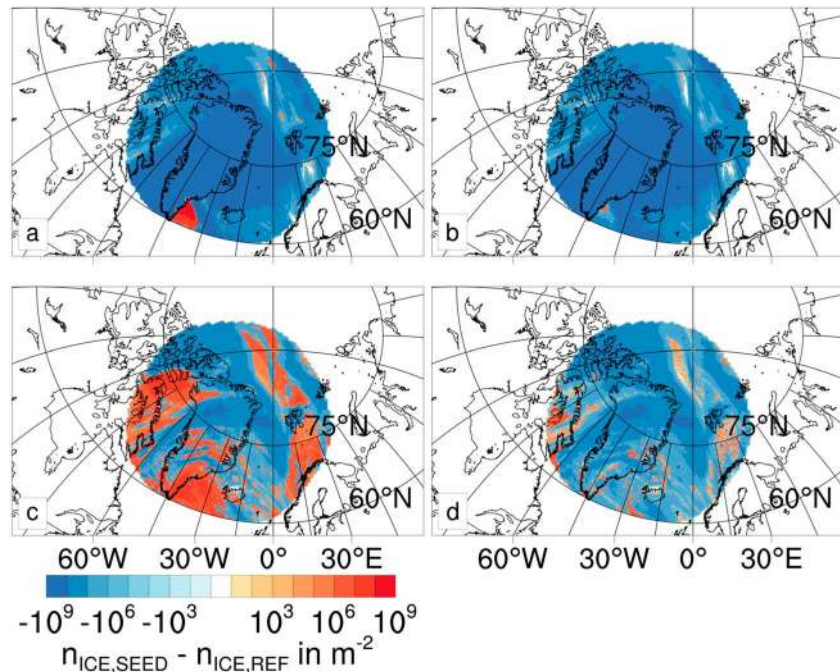

Figure 9. Difference in column-integrated n_{ICE} compared to *REF* for *SEED* (a, c) and *TRGT* (b, d) in regions with $T < 235$ K (a, b) and $235K < T < 273$ K (c, d) averaged over the entire domain and simulation time.
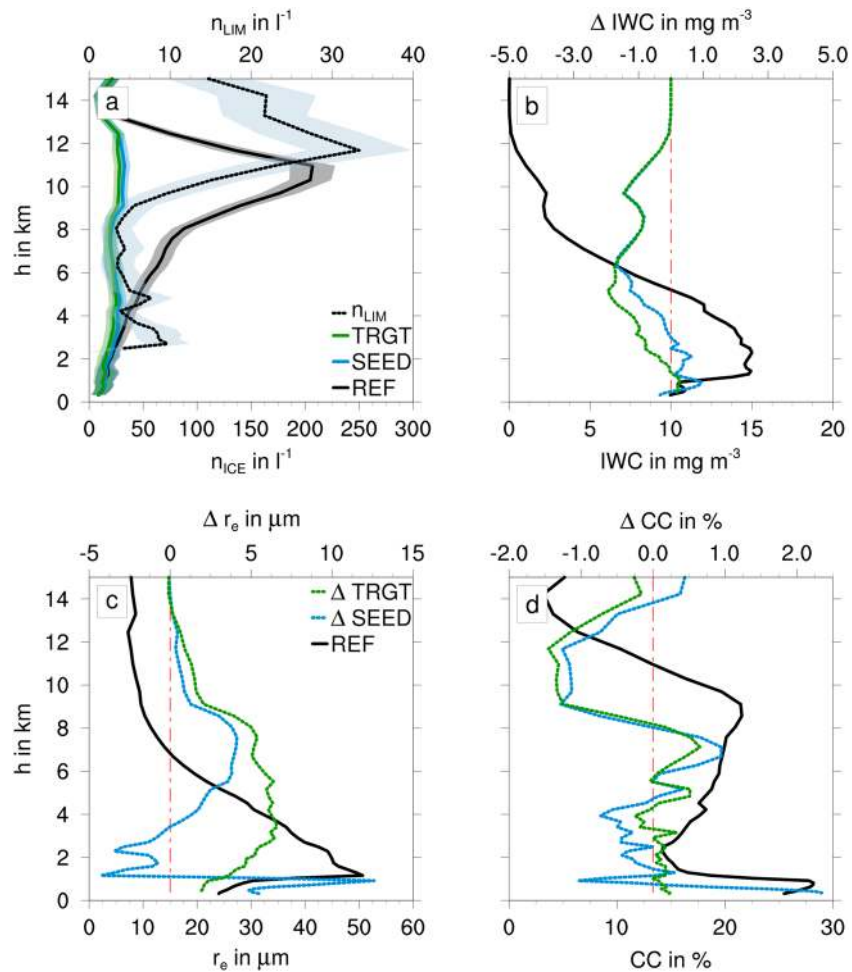
Figure 10. Comparison of ice cloud properties averaged over the entire domain and simulation time for reference simulation (black) and seeding strategies *SEED* (blue) and *TRGT* (green). (a) n_{ICE}. (b) IWC. (c) r_e. (d) Cloud cover. Solid lines are absolute values; dotted lines represent differences compared to the reference simulation. Shaded areas indicate standard deviations. Note that in (a) only absolute values are depicted; the black dotted line is n_{LIM} for the reference simulation. IWC = ice water content.

nucleation (Barahona & Nenes, 2009b). At altitudes where high values of n_{ICE} are present, n_{LIM} is lower than about 5 L^{-1} (at 8 km) and increases strongly with height. The optimal n_{SEED} can be chosen in accordance to n_{LIM}. In this study, seeding particles are assumed to be similar to mineral dust, with a freezing efficiency of only about 0.05 (Pruppacher & Klett, 1997). Therefore, a reasonable agreement is found for effective values of n_{SEED} in this study being about 20 times higher compared to former studies assuming perfect INP, that is, having a freezing efficiency of 1 (Gasparini et al., 2017; Storelvmo et al., 2013). In these studies, optimal values n_{SEED} were found ranging from 10 and 100 L^{-1}.

In REF, the highest values of n_{ICE} exceeding 200 L^{-1} are found at altitudes between 8 and 13 km (Figure 10a). Both seeding strategies lead to a remarkable reduction of n_{ICE} throughout nearly the entire atmosphere between 3- and 13-km height. In the levels with the highest values of n_{ICE} in REF, seeding leads to ice crystal number concentrations below 50 L^{-1}, corresponding to a reduction to about 25% of n_{ICE} in REF.

Interestingly, the reduction of n_{ICE} in SEED is stronger than in TRGT, that was designed to be of the higher efficiency. Apparently, seeding according to TRGT can only inhibit homogeneous nucleation where it is about to occur, whereas with SEED, additionally artificial cirrus clouds are formed in regions where super-saturation is too low for homogeneous nucleation, thus on one hand leading to additional cirrus clouds but concomitantly reducing supersaturation, hence inhibiting homogeneous nucleation further downstream.
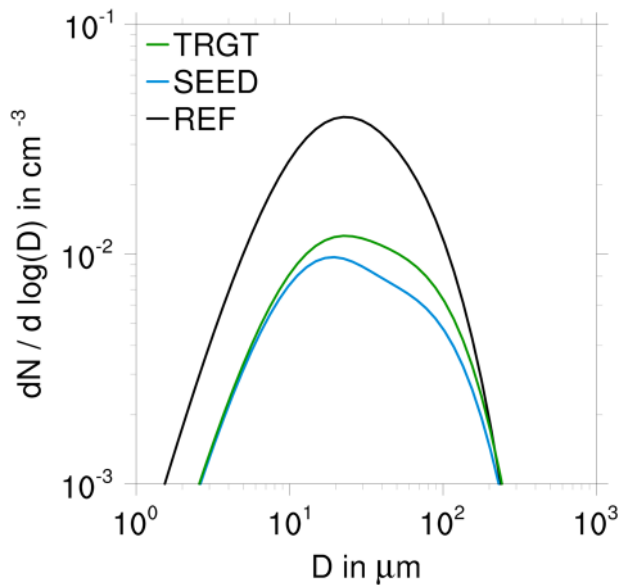
Figure 11. Ice crystal size distribution in cirrus levels (8–13 km) averaged over the entire domain and simulation time for reference simulation (black) and different seeding strategies (blue and green).

Besides a strong reduction of n_{ICE}, also remarkable changes in IWC are found with seeding in both scenarios (Figure 10b). As described above, heterogeneous ice nucleation due to seeding and subsequent sedimentation reduce IWC by about 2.5 to 1.5 mg/m^3, corresponding to a reduction of up to 60%.

Besides reducing n_{ICE} and IWC of ice crystals in cirrus clouds, it is furthermore desirable to increase the ice crystal effective radius (r_e) of the remaining ice crystals, as increased mean ice crystal sizes lead to a decreased extinction coefficient and thus reduced cloud optical thickness. In REF, r_e in the cirrus region is around 10 μm (Figure 10c). Contrary to former studies, a small increase due to seeding is found in both seeding scenarios. So far, r_e was found to either strongly increase (Storelvmo et al., 2013) or rather decrease (Gasparini & Lohmann, 2016). The minor increase of about only 1 μm, compared to up to tenfold values in Storelvmo et al. (2013), can be attributed to generally smaller values due to different parameterizations used for calculating both r_e and the sedimentation of ice crystals. Apart from this, although n_{ICE} obviously is reduced strongly (Figure 10a), only a small absolute reduction in IWC is found, as values are low already in REF (Figure 10b).

However, the response of ice crystal properties to seeding is more complex than only the average decrease in n_{ICE} and IWC leading to an increase in r_e. Therefore, in Figure 11, size distributions of ice crystals, averaged over the cirrus region, are depicted. Consistent with the findings above, the reduction in number concentration is much larger than the average growth in size, as for both seeding strategies, peak number concentrations decrease strongly, whereas the shift to larger mean sizes is hardly evident. Nevertheless, number concentrations of ice crystals with very small sizes decrease strongly with TRGT and even more with SEED. In contrast, number concentrations of ice crystals larger than about 200 μm are reduced only marginally, and compared to the overall distinct decrease, ice crystals number concentrations with sizes above 20 μm are less strongly reduced, indicating a higher frequency of occurrence of larger crystals, thus broadening the distribution toward larger sizes. This effect is more pronounced when applying the TRGT seeding strategy that, by construction, removes more of the small ice crystals arising from homogeneous nucleation.

Former studies pointed at the importance of reducing cirrus cloud cover (*CC*) with seeding (Gasparini et al., 2017; Mitchell & Finnegan, 2009; Storelvmo et al., 2013). However, compared to those, in both SEED and TRGT, CC decreases only marginally in cirrus levels (Figure 10d). However, in the simulations presented here, it is nearly impossible to reduce CC by seeding, as the integration time of 24 hr is too short for sedimentation of smaller ice crystals dehydrating the upper troposphere to a significant extent. Furthermore, a certain contribution from the unseeded lateral boundaries leads to on average diminishing
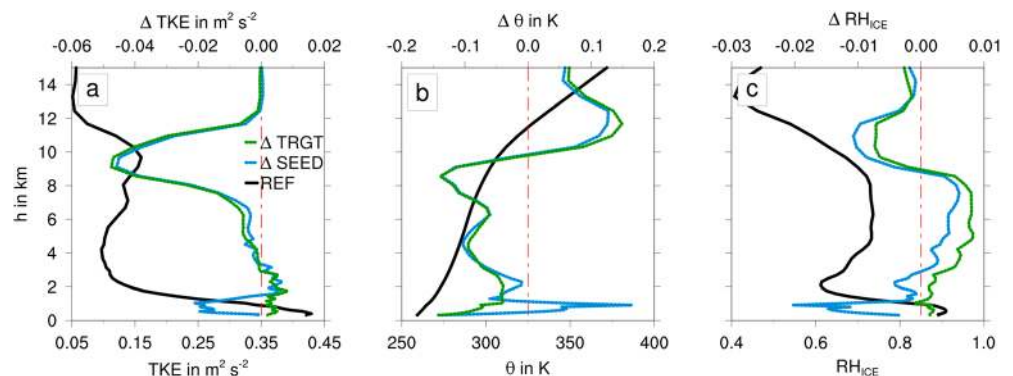

Figure 12. Changes of TKE (a), potential temperature (b), and RH$_{ICE}$ (c) averaged over the entire domain and simulation time for reference simulation (black) and seeding strategies *SEED* (blue) and *TRGT* (green). Solid lines are absolute values; dotted lines represent differences compared to the reference simulation. TKE = turbulent kinetic energy.
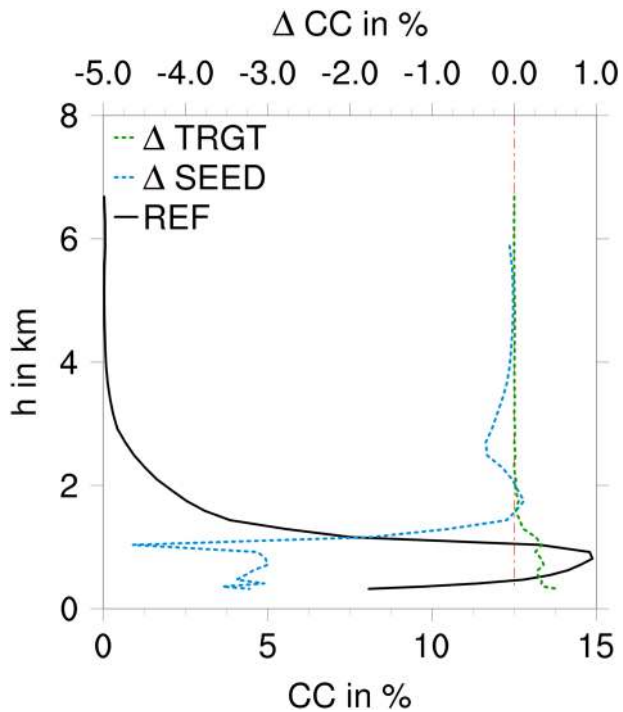
Figure 13. Comparison of liquid (mixed phase) cloud cover averaged over the entire domain and simulation time for reference simulation (black) and seeding strategies *SEED* (blue) and *TRGT* (green). The solid line shows absolute values; dotted lines represent differences compared to the reference simulation. CC = cloud cover.

reductions of humidity (Figure 12c). In addition, the seeding aerosol number concentrations change with height but are horizontally homogeneously distributed. Therefore, even when n_{SEED} is high enough to suppress homogeneous nucleation, heterogeneous nucleation still occurs and thus the reduction of cloud cover is small.

In a former study, although in the global mean, increased convective activity due to seeding cirrus clouds was found (Gasparini et al., 2017). However, during Arctic winter, characterized by low temperatures and lack of incoming solar radiation, convective activity is low (Figure 12a) and the troposphere is stably stratified (Figure 12b). In contrast to Gasparini et al. (2017), in the upper troposphere, convective activity in both SEED and TRGT is reduced by up to one third (Figure 12a) and stability is slightly increased (Figure 12b).

This hints at a self-enhancing feedback mechanism. Thinning cirrus clouds reduces cloud top cooling, causing increased stability and less turbulence. Small-scale, turbulent fluctuations in w build up supersaturation high enough for homogeneous nucleation; hence, reducing the turbulent activity can aid in suppressing homogeneous nucleation and thereby leading to optically thinner cirrus clouds.

4.3. Impact on Mixed-Phase Clouds

In most of the former studies investigating the effects of introducing INP for cirrus seeding, the response of mixed-phase clouds was not considered (Gasparini & Lohmann, 2016; Storelvmo & Herger, 2014; Storelvmo et al., 2013). In this study, seeding aerosol particles only act as INP, so no direct impact on activation of cloud droplets is possible. Nevertheless, due to the presence of additional INP at lower levels, combined with increased sedimentation of ice crystals from above, second-order changes within mixed phase clouds are occurring.

In Figure 10b, IWC in REF is highest at lower altitudes just above the PBL and strongly decreases with height. At altitudes between 3.5 and 9 km, as in the cirrus region, heterogeneous ice nucleation due to seeding and subsequent sedimentation of formed ice crystals leads to a decrease in IWC. As homogeneous nucleation at these altitudes occurs less frequently than above, thinning out ice clouds via suppression of homogeneous nucleation occurs more rarely in TRGT compared to SEED.

At altitudes between 5 and 8 km, ice cloud cover sightly increases in SEED, as at these altitudes heterogeneous nucleation forms artificial cirrus clouds. With regard to achieving maximum cooling, any additional CC reduces the primary cooling effect, as outgoing LW radiation is trapped. However, the compensating effect is smaller, the further down the clouds form, as lower-lying clouds emit LW radiation at higher temperatures than colder high-level cirrus clouds.

A slight increase of IWC is found in SEED at lower altitudes up to 3.5 km, as the seeding aerosol, although only present in low number concentrations, leads to additional artificial ice crystal formation in mixed-phase clouds. However, compared to changes in n_{ICE} at higher altitudes, hardly any change can be found here (Figure 10a), as n_{SEED} is rather low. Nonetheless, within these low altitudes, more humidity is available than above, amplifying growth by deposition as well as glaciation effects, that is, riming of cloud droplets onto preexisting ice crystals, as well as the Wegener-Bergeron-Findeisen process (e.g., Fan et al., 2011). In SEED, this process effectively removes cloud droplets, resulting in a strong decrease in CC of liquid clouds of up to 4.5% within the PBL, corresponding to a reduction by one third (Figure 13). Notably, also the highest altitude where cloud droplets occur at all decreases by about 1 km. Longer integration time and hence mounting redistribution of ice crystals from higher altitudes due to sedimentation is expected to reduce liquid cloud cover even further.

As riming occurs regardless of the cloud droplet size, hardly any change in droplet size distributions is found (not shown). Furthermore, changes in n_{CLD}, LWC, and r_e are small and without a clear trend (not shown).
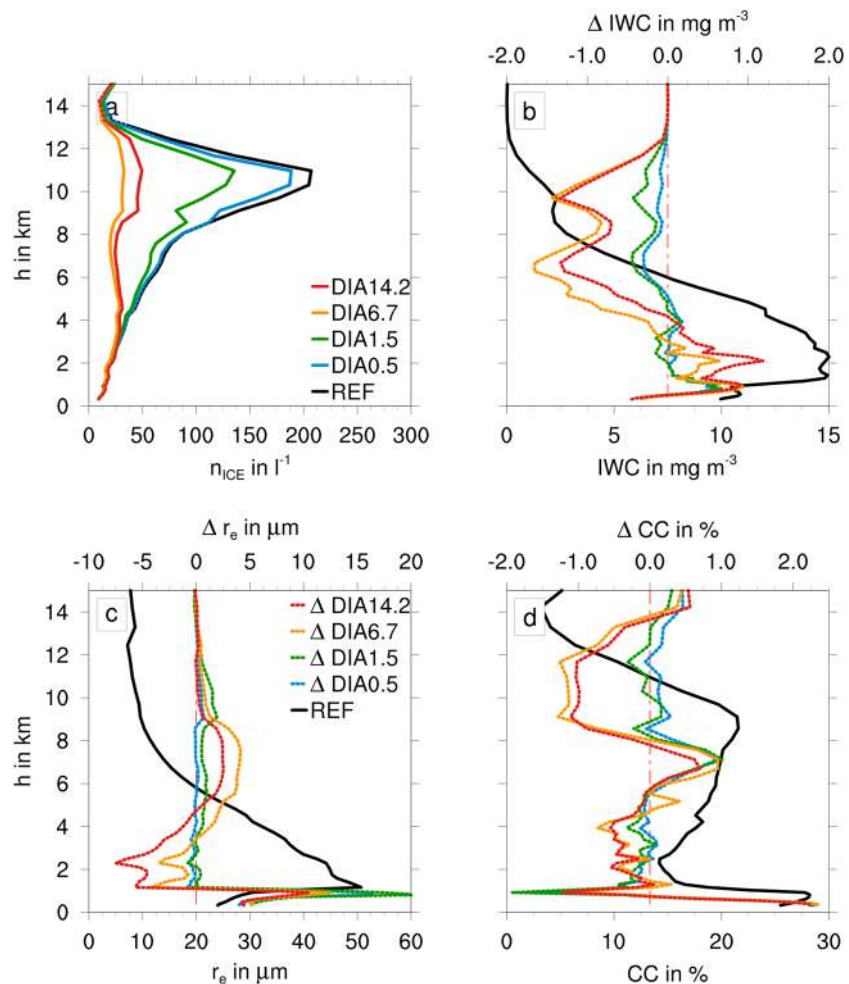
Figure 14. Comparison of ice cloud properties averaged over the entire domain and simulation time for reference simulation (black) and simulations with n_{SEED} according to Figure 6 and various d_{SEED} (colors). (a) n_{ICE}. (b) IWC. (c) r_e. (d) Cloud cover. Solid lines are absolute values; dotted lines represent differences compared to the reference simulation. Note that in (a) only absolute values are depicted. IWC = ice water content; CC = cloud cover.

In TRGT, seeding aerosol is active only where necessary to inhibit homogeneous nucleation; hence, barely any change in IWC can be found at lower levels (Figure 10b), as heterogeneous nucleation is dominant due to both higher temperatures and higher concentrations of n_{DUST} inhibiting homogeneous nucleation already. Especially, instead of a reduction in liquid CC at very low levels, even a small increase is found (Figure 13). This strengthens the finding that the secondary effect of seeding is due to introducing additional INP changing ice crystal properties and frequency of occurrence also at low altitudes.

4.4. Sensitivity to Concentration and Size of Seeding Aerosol

Both the amount and size of the seeding aerosol particles crucially determine the response of both cirrus and mixed-phase clouds to seeding. The efficiency of INP increases strongly with their surface area (Hoose & Möhler, 2012) as the latter increases quadratically with particle size. However, with respect to seeding of cirrus clouds, finding the optimal size of the seeding aerosol particles is difficult. Using larger, more efficient particles, n_{SEED} can be lower than with smaller particles. Hence, as larger particles sediment faster with the fall speed increasing approximately quadratically, too, the effects of increasing efficiency and increasing sedimentation might compensate each other (Gasparini et al., 2017). However, in this study, the aerosol particles neither get advected or sediment nor they are scavenged during the nucleation process; n_{SEED} remains constant. This, to some extent, mimics a consecutive injection of seeding aerosol to retain an already built up homogeneously distributed profile.
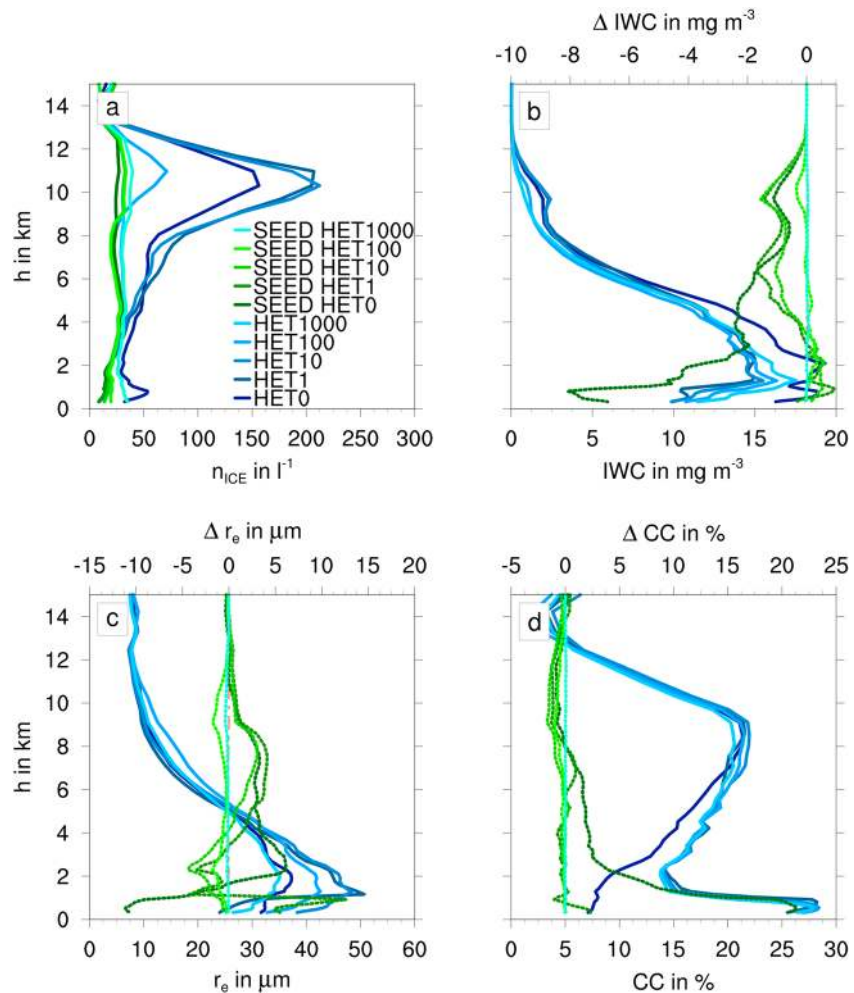
Figure 15. Comparison of ice cloud properties for different dust aerosol concentrations averaged over the entire domain and simulation time for reference simulations (blue) and simulations with n_{SEED} according to Figure 6 and $d_{\text{SEED}} = 6.7\ \mu$m. (a) n_{ICE}. (b) IWC. (c) r_e. (d) Cloud cover. Solid lines are absolute values; dotted lines represent differences compared to the corresponding reference simulation. Note that in (a) only absolute values are depicted; the dotted lines are n_{LIM} for the reference simulations. IWC = ice water content; CC = cloud cover.

Despite the higher efficiency of larger particles, from a technical implementation point of view, smaller particles and thus less total mass might be favored. Therefore, the impact of varying d_{SEED}, listed as *DIA0.5* until *DIA14.2* in Table 1, is examined. As the choice of values for d_{SEED} is somewhat arbitrary, the same values as for mineral dust are assumed. In addition, the effect of very small ($d_{\text{SEED}} = 0.5\ \mu$m) particles is investigated in DIA0.5. For simplicity and better comparison, the same profile of n_{SEED} according to Figure 6 is assumed for all scenarios.

In Figure 14a, averaged vertical profiles of n_{ICE} in response to seeding with changing d_{SEED} are depicted. As expected, reduction in n_{ICE} within the altitudes where cirrus clouds are present is largest for the larger d_{SEED}. However, the largest aerosol particles with $d_{\text{SEED}} = 14.2\ \mu$m (red) seem to be slightly less efficient than the second largest ones ($d_{\text{SEED}} = 6.7\ \mu$m, orange) with respect to reducing n_{ICE} (Figure 14a), IWC (Figure 14b), and CC (Figure 14d) as well as increasing r_e (Figure 14c) in the cirrus region. As d_{SEED} is more than doubled from DIA6.7 to DIA14.2, the nucleation effectivity increases by a factor of 4. As furthermore n_{SEED} is the same in both scenarios, consequently four times as many ice crystals can be formed in DIA14.2 compared to DIA6.7, leading to a smaller net reduction in n_{ICE}. Apparently, for DIA14.2, the prescribed n_{SEED} is too large, resulting in a beginning overseeding. As the excess water vapor is distributed on more, and initially larger, ice crystals compared to DIA6.7, their subsequent growth is reduced.
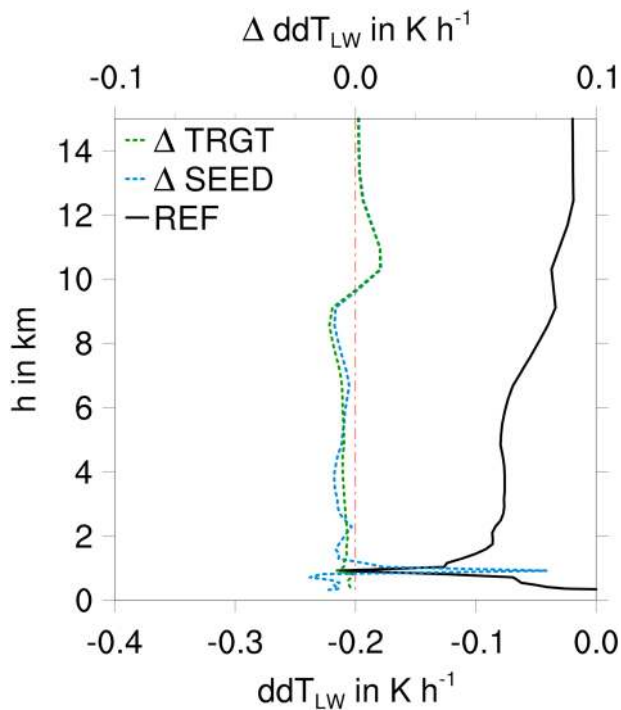
Figure 16. Comparison of the longwave heating rates averaged over the entire domain and simulation time for reference simulation (black) and seeding strategies *SEED* (blue) and *TRGT* (green). The solid lines show absolute values; dotted lines represent differences compared to the reference simulation.

In contrast, with smaller d_{SEED} of 0.5 and 1.5 μm, only a moderate reduction of n_{ICE} is found in Figure 14a, as both scenarios are unable to suppress homogeneous nucleation entirely (not shown). Consequently, also the reduction in IWC (Figure 14b) and CC (Figure 14d) and the increase of r_e are less distinct compared to seeding with larger particles in Figure 14c.

At lower altitudes, where mixed-phase clouds are present, changes in cloud microphysical properties of both liquid and frozen hydrometeors are strongest when injecting the largest seeding aerosol particles (Figure E1). Here, the higher water vapor content is not limiting the growth of ice crystals formed by seeding. Consequently, changes within the liquid phase as described in section 4.3 are enhanced when using the seeding aerosol particles with the largest d_{SEED}.

4.5. Sensitivity to Background Mineral Dust

As discussed in section 3.1, varying the background mineral dust number concentrations has a certain impact on the fraction of homogeneous to heterogeneous nucleation and therefore on n_{ICE}. This in turn governs the efficacy of seeding that can only have the desired outcome when, in the predominant absence of natural aerosol, additional seeding aerosol can inhibit homogeneous nucleation. Therefore, the scenarios listed in Table 1 are compared with corresponding simulations including seeding aerosol according.

As the background dust concentrations are generally low in the UTLS region (Figure 2a), even hundredfold values (HET100) are too low to inhibit homogeneous nucleation. However, homogeneous nucleation is reduced strongly, hence leading to lower values of n_{ICE} in the cirrus regime, when increasing n_{DUST} by a factor of 10^3 (HET1000).

It is important to note that absence of mineral dust (*HET0*) does not lead to the highest n_{ICE}. This is due to homogeneous nucleation bursts reducing supersaturation strongly that in turn can negatively impact environmental conditions for nucleation downstream and additionally leading to enhanced evaporation of ice crystals in now subsaturated air masses. Furthermore, although only homogeneous nucleation can happen here, the results are strongly determined by the initial values of n_{ICE} at initialization and when updating the boundaries obtained by dividing the initial IWC by a constant mean mass for single ice crystals. Apparently, the chosen value here leads to a certain inhibition of in-cloud homogeneous nucleation that only can happen when very few preexisting ice crystals are present.

However, with seeding, n_{ICE} in the cirrus regime is reduced to similar values independently from n_{DUST} (Figure 15a). Likewise, IWC is reduced by similar amounts (Figure 15b). Therefore, seeding cirrus clouds proves to yield the desired effect over a rather wide range of possible values for n_{DUST}, although it is crucial to note that the efficacy scales strongly with background aerosol concentrations.

As n_{DUST} is already high at low altitudes, increasing the latter strongly by scaling reduces liquid cloud cover (Figure E2). Here, enhanced riming rates are already high in the reference simulations, that is, additional seeding aerosol and sedimented ice crystals have a negligible impact.

4.6. Impact on Heating Rates

Changes in cloud cover, effective radius, and IWC and LWC have an impact on the radiative fluxes that can be characterized by their divergence, resulting in changing heating rates. In REF, the averaged vertical profile of LW cooling rates (ddT_{LW}) in Figure 16 has distinct maxima just above the major layers of both ice and liquid clouds characterized by cloud cover (Figures 10d and 13) as well as IWC (Figure 10b) and LWC (not shown). Notably, the peak of cooling within the PBL is found with similar values also during Arctic spring and fall (Harrington et al., 1999). The impact of cirrus clouds is in agreement with theoretical studies assuming similar IWC of cirrus clouds (Schmidt & Garrett, 2013) but underestimated compared to other studies using either different radiative transfer algorithms (Baer et al., 1996) or rather observation-based calculations focusing on convective cirrus in the tropics (McFarlane et al., 2007). Discrepancies compared
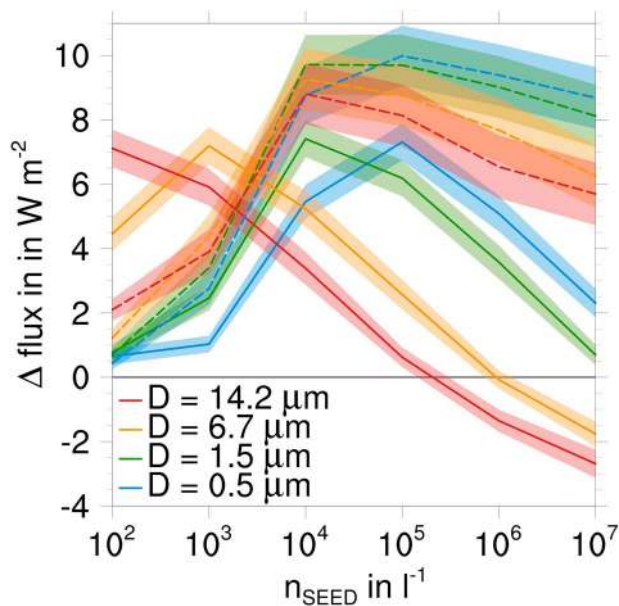
Figure 17. Changes in outgoing longwave net flux at top of the atmosphere (solid) and surface (dashed) due to seeding for different combinations of n_{SEED} and d_{SEED} averaged over the entire domain and simulation time. Shaded areas represent standard errors.

to the latter, however, might be explained by much lower temperatures during the Arctic winter of both the surface and the air above, causing only small total LW fluxes.

For SEED and TRGT, ddT_{LW} is depicted as difference to the values of REF in Figure 16. For both scenarios, a net warming, that is, decreasing LW cooling is found within the cirrus region.

Arctic mixed-phase clouds are self-regulating due to buoyancy mixing generated by cloud top cooling (e.g., Morrison et al., 2012). Overlying cloud layers such as cirrus suppress this cooling, that is, weakening the stratocumulus (e.g., Verlinde et al., 2013). Therefore, a positive and stabilizing feedback on mixed-phase clouds could be induced by thinned cirrus clouds leading to enhanced cloud top cooling at altitudes below. This effect can be found in TRGT, indicated by slightly stronger LW cooling at low altitudes (Figure 16) and a small increase in both liquid (Figure 13) and ice (Figure 10d) CC. In SEED, however, removal of cloud droplets by riming and hence strong glaciation and removal of the liquid phase dominates.

4.7. Impact on Radiation

A number of simulations were carried out varying both n_{SEED} and d_{SEED}. The resulting changes in OLR averaged over the entire integration time and simulation domain are shown as solid lines in Figure 17. Variation in n_{SEED} is performed by simply scaling the profile shown in Figure 6. The values of n_{SEED} on the abscissa of Figure 17 mark the "peak concentrations" of the concentration profiles at altitudes of about 12 km. The SEED scenario discussed in sections 4.2 and 4.3 with $n_{SEED} = 10^3$ L^{-1} and $d_{SEED} = 6.7$ μm is among the most effective choices, increasing OLR by 7.00 ± 0.31 W/m^2. Due to its smaller efficacy, the increase in OLR in the idealized TRGT scenario is only 5.80 ± 0.30 W/m^2. A major concern in former studies is so-called overseeding, that is, a positive radiative forcing resulting from prolonged lifetime or decreasing r_e of cirrus clouds due to seeding (Gasparini & Lohmann, 2016; Storelvmo & Herger, 2014; Storelvmo et al., 2013). However, in this study, negative changes in the net OLR at TOA occur only when injecting both larger and very high number concentrations of seeding aerosol particles. Notably, this effect is found only with unrealistic values of n_{SEED} as high as 10^5 L^{-1}, comparable to the number concentrations of ubiquitous sulfate droplets. As expected, when using larger aerosol particles, lower number concentrations are sufficient to achieve a similar enhancement of OLR compared to seeding with smaller particles.

Increasing upward fluxes of LW radiation at the Earth's surface cools the latter. Keeping in mind that the overall cooling effect of cirrus thinning on the climate system can be amplified by exploiting the self-enhancing polar sea ice albedo feedback (Holland & Bitz, 2003), this is a desired secondary effect of cirrus seeding. As discussed before, besides thinning cirrus clouds, injecting seeding aerosol also reduces mixed-phase clouds. Therefore, also, the net flux of LW radiation at the Earth's surface (SFC) is examined, depicted as dashed lines in Figure 17.

Here, the change in the surface LW net flux in the SEED scenario is 4.23 ± 0.39 W/m^2. As for TRGT, in which hardly any changes in mixed-phase clouds occur, the increase in LW net flux at the surface is only 1.10 ± 0.05 W/m^2. For n_{SEED} up to 10^3 L^{-1}, larger aerosol particle sizes lead to stronger increase in net LW radiation flux at the surface, as liquid cloud cover is reduced more strongly than with smaller sizes. In contrast, for even larger values of n_{SEED}, smaller seeding aerosol particles are more effective. This is predominantly due to enhanced redistribution of water vapor to the ice phase and riming, which strengthens the reduction in liquid cloud cover. For larger, hence more effective, INP, this effect is outweighed by an overseeding effect, that is, the reduction in ice crystal r_e resulting from strong increase of n_{ICE}.

The averaged changes in radiative fluxes for the simulation with modified mineral dust concentrations mentioned in section 4.5 are listed in Table 2. Here, changes in both OLR at TOA and SFC are large for the cases without (*SEED HET0*) or with low n_{DUST} (*SEED HET1*, *SEED HET10*). Here, seeding has a large impact on both cirrus clouds and on mixed-phase clouds. In case of higher mineral dust concentrations,

Table 2
Changes in Longwave Radiative Fluxes (W/m^2) Averaged Over Entire Domain and Simulation Time for the Sensitivity to Mineral Dust Background Concentrations

Simulation	$\varDelta$ net, TOA	$\varDelta$ net, SFC
SEED HET0	-6.90 ± 0.29	-6.95 ± 0.07
SEED HET1	-6.45 ± 0.27	-4.11 ± 0.38
SEED HET10	-6.48 ± 0.28	-0.81 ± 0.06
SEED HET100	-0.91 ± 0.09	-0.04 ± 0.02
SEED HET1000	0.34 ± 0.01	0.08 ± 0.01

Note. TOA = top of the atmosphere; SFC = surface.

efficacy of the method decreases strongly. For the extreme case assuming $10^3 \times n_{\mathrm{DUST}}$ (*SEED HET1000*), except for a reduction in n_{ICE}, properties of both ice clouds (Figures 15a–15d) and liquid clouds (Figure E2) remain merely unchanged. Consequently, no cooling, but even a slight warming is found. This finding highlights the importance of knowledge about a realistic aerosol background for a correct assessment of the method's efficiency.

Finally, a rough approximation of the seeding aerosol mass necessary to establish a vertical profile, as depicted in Figure 6, for different choices of n_{SEED} and d_{SEED} is presented in Figure 18. The lines read as either column-integrated mass per square meter for the left axis or as total mass necessary to seed the entire Arctic region (i.e., north of 60°N). In Figure 17, a maximum cooling at TOA of about 7.5 W/m^2 occurs for several different pairs of n_{SEED} and d_{SEED} relatively independent of the actual size and concentration of the seeding aerosol, that is, with $10^3 \mathrm{L}^{-1}$ and 6.7 μm, 10^4 L^{-1} and 1.5μm, and 10^5 L^{-1} and 0.5 μm. Those values result in a similar column-integrated aerosol loading of about 10^{-3} g/m^2 corresponding to about 10^7 to 10^8 kg of seeding material required for the entire Arctic region. As larger aerosol particles are more efficient INP due to their higher number of active sites (Kiselev et al., 2017), lower concentrations are sufficient compared to smaller particles. This hints at an approximately constant total number of active sites throughout the different scenarios. A similar pattern can be found for the threshold toward "overseeding", that is, a decrease in OLR at TOA instead of an increase. Here, the critical column-integrated mass is about 10 g/m^2 or rather 10^{11} to 10^{12} kg mass in total. These connections might provide a possible simple estimate of the efficacy of seeding Arctic cirrus clouds. However, a less distinct correlation can be found for the maximum change of the surface LW net flux that rather seems to depend on n_{SEED} than on the total mass.
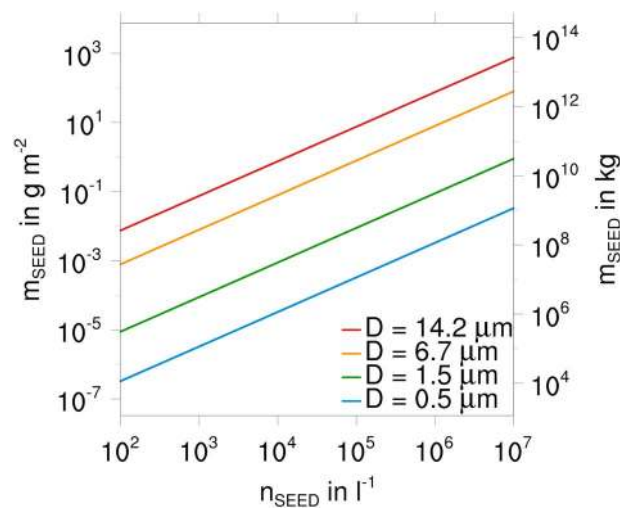

Figure 18. Mass of seeding aerosol for different combinations of n_{SEED} and d_{SEED}. Left axis represents column-integrated mass per square meter, right axis represents total aerosol mass for the entire Arctic region (i.e., north of 60°N).

5. Conclusion

In this study, cloud-resolving simulations were performed with the atmospheric modeling system ICON-ART coupled with a comprehensive and detailed cloud microphysical scheme.

Comparison to measurement data obtained from several sources yield reasonable agreements. Especially, the distribution of humidity, which strongly determines cloud formation in the upper troposphere, is reproduced well compared to data gathered during the Polar Stratosphere in a Changing Climate campaign by GLORIA.

The model is applied to clarify the cloud microphysical processes accompanied by injecting artificial aerosol particles into the UTLS region with the aim of modifying cirrus clouds in the framework of climate engineering. Focusing on the hibernal Arctic region has turned out to be most promising; as here, due to lack of incoming solar radiation, cirrus clouds have only warming effects, and removing or thinning them yield the maximum possible cooling effect. Former studies of cirrus thinning were performed with either a simple proxy for actual seeding and/or used GCMs with much coarser horizontal resolutions (Gasparini et al., 2017; Muri et al., 2014; Storelvmo & Herger, 2014) focusing on anomalies in global radiative forcing.

In addition, in this study, a somewhat more realistic scenario of injecting seeding aerosol with ice nucleation properties like mineral dust is investigated by applying a vertical profile of seeding aerosol number concentrations obtained from a separate simulation assuming injection of the seeding material along commercial flight trajectories and subsequent dispersion into the Arctic region. However, also in this study, the seeding aerosol particles are prescribed and not removed via nucleation or sedimentation.

The primary effect of seeding, that is, the reduction of ice crystal number concentrations and IWC is found to be predominant compared to only small increases of the ice crystal effective radii and minor reductions in cirrus cloud cover. Furthermore, it turns out that only inhibiting homogeneous nucleation, where it is about to occur (TRGT), is less effective than seeding everywhere (SEED). The latter scenario admittedly leads to formation of additional cirrus clouds but concomitantly reduces supersaturation, hence inhibiting homogeneous nucleation further downstream. Those findings are partly contradictory to former studies that found either large changes in IWC and r_e (e.g., Storelvmo & Herger, 2014) or a slight increase of the latter (Gasparini & Lohmann, 2016).

The impact of cirrus seeding on the LW radiative fluxes is twofold. First, an increase in OLR at the TOA occurs due to reduced ice crystal number concentrations within cirrus clouds. This effect is present over a wide range of assumed number concentrations and sizes of the seeding aerosol and maximized for number concentrations of 10^3 L^{-1} and rather large particles. Furthermore, an amplifying secondary effect is found. Mostly due to the enhanced heterogeneous nucleation on seeding aerosol particles present also at lower altitudes, a redistribution of water vapor in favor of the latter and enhanced riming of cloud droplets occurs, leading to a reduction or glaciation of originally mixed-phase clouds. Reduced liquid cloud cover leads to enhanced upward LW fluxes at Earth's surface, hence generating additional cooling there. Furthermore, throughout the simulations, the efficacy of seeding on cirrus clouds is only weakly sensitive to changes in mineral dust concentrations, as long as the latter are not increased to very high values. In contrast, the observed reduction in liquid cloud cover only occurs with low background mineral dust concentrations. For low number concentrations of the seeding aerosol, efficacy drops quickly. In contrast, overseeding is hardly found, with the exception of very large aerosol particles and very high number concentrations close to the concentration of sulfate aerosol droplets responsible for homogeneous nucleation.

Appendix A: Aerosol in ICON-ART

The particle size distribution of both mineral dust and sea salt aerosol is approximated by three log-normally distributed modes associated with prognostic number concentrations and mass mixing ratios. Keeping the standard deviations σ_i constant during the simulation, the modes' mean diameter is a diagnostic variable being able to change due to aerosol dynamical processes like sedimentation, dry deposition, and washout. A detailed description of parameterizations for mineral dust emission can be found in Rieger et al. (2017). The emission fluxes of sea salt aerosol are calculated online depending on wind speed and temperature (Lundgren et al., 2013). An overview of the initial values for the modal parameters of mineral dust can be found in Table A1.

Table A1
Initial Parameters of Mineral Dust

Mineral dust	Mode A	Mode B	Mode C
d_i (μm)	1.5	6.7	14.2
σ_i	1.7	1.6	1.5

d_i is the median diameters of the specific mass emission for mode i; σ_i is the standard deviation for mode i.

Appendix B: Cloud Microphysics

For this study, ICON-ART is coupled with a comprehensive two-moment cloud microphysical scheme following Seifert and Beheng (2006). The scheme considers six hydrometeor classes (cloud droplets, ice, rain, snow, graupel, and hail) that are described by prognostic budget equations for both mass and number concentrations. The particle size distribution of each class is characterized by a generalized Γ distribution. The shape of particles in each class is approximated using a power law formulation. The mean size D (in meters) of a single particle is related to its mean mass m (in kilograms) via a mass-size relation:

$$D = a_{\text{geo}} m^{b_{\text{geo}}} \tag{B1}$$

An overview of the shape coefficients a_{geo} and b_{geo} for all hydrometeor classes can be found in Seifert and Beheng (2006).

Changes in the liquid phase are considered by condensational growth, accretion, autoconversion, self-collection, break up, and freezing, whereas frozen hydrometeors undergo diffusional growth, aggregation, self-collection, riming, ice multiplication, and melting.

To obtain realistic rates for the formation of ice crystals, a careful description of the competition between homogeneous and heterogeneous nucleation of ice crystals is required. This is realized via the parameterization after Barahona and Nenes (2009b). Besides temperature, supersaturation, and updraft velocity, homogeneous nucleation depends only on number concentration (n_{HOM}) and diameter (d_{HOM}) of small liquid aerosol droplets (Koop et al., 2000). Assuming ubiquitous presence of such particles (Köhler & Seifert, 2015), constant values for $n_{\text{HOM}} = 1,000$ cm^{-3} and $d_{\text{HOM}} = 200$ nm are prescribed throughout the atmosphere.

To parameterize heterogeneous nucleation, the formulation after Phillips et al. (2013) is applied. In this study, only mineral dust is considered as possible INP, as this species both has effective ice-nucleating properties and prevails over most of the atmosphere. Other species like soot, organic, or metallic particles might therefore be neglected in modeling studies (Cziczo et al., 2013).

$$\sigma_{\text{TKE}} = f_w \sqrt{\text{TKE}} \tag{B2}$$

As even with a relatively high spatial resolution of 5 km parts of the dynamical structures decisive for cloud formation remain unresolved, a Gaussian distribution based on turbulent kinetic energy (TKE) to account for the subgrid scale variability of the vertical velocity is applied (equation (B2)) after Lohmann et al. (1999), who proposed $f_w = 0.7$ for use in coarse-resolution global models, whereas Rieger et al. (2015) found $f_w = 0.3$ yielding better results in higher-resolution ICON-ART simulations of a midlatitude spring episode compared to measurements. The latter are found to yield reasonable results also for the simulations presented in this study.

For the formation of cloud droplets, a parameterization based on classical activation theory is used (Fountoukis & Nenes, 2005). This parameterization calculates the activation of log-normally distributed aerosol species at the maximum supersaturation possible. The latter is determined by the diabatical cooling rate, dependent on vertical movement and thermodynamical state. The decelerated growth of giant cloud condensation nuclei (Barahona et al., 2010) is considered as well as the activation of insoluble particles via Frenkel-Halsey-Hill adsorption theory (Kumar et al., 2009). When using this configuration with a two-moment scheme, it is important to distinguish whether activation takes place either within a preexisting cloud or at its base or rather forming an entirely new cloud (Bangert et al., 2012).
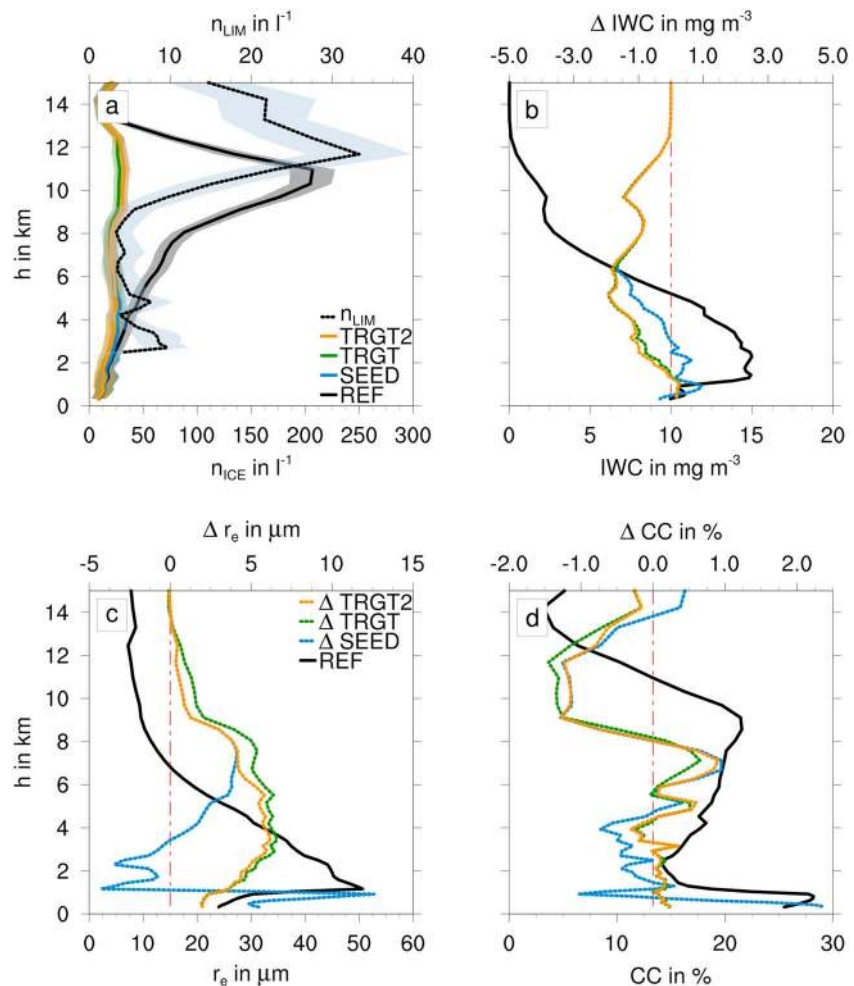
Figure D1. Comparison of ice cloud properties averaged over the entire domain and simulation time for reference simulation (black) and seeding strategies *SEED* (blue) and *TRGT* (green). (a) n_{ICE}. (b) IWC. (c) r_e. (d) Cloud cover. Solid lines are absolute values; dotted lines represent differences compared to the reference simulation. Shaded areas indicate standard deviations. Note that in (a) only absolute values are depicted; the black dotted line is n_{LIM} for the reference simulation. IWC = ice water content; CC = cloud cover.

Appendix C: Radiation

The radiative fluxes in ICON-ART are calculated using the Rapid Radiative Transfer Model (RRTM) (Mlawer et al., 1997). The interactions of mineral dust and sea salt with the radiative fluxes realized in ICON-ART are described in detail in Rieger et al. (2017) and Gasch et al. (2017). To account for the impact of hydrometeors on radiation, cloud optical properties are calculated based on the effective radius (r_e) following Stevens et al. (2013). This formulation only considers the mass mixing ratio of cloud ice and cloud droplets, respectively, designed to be used together with a single-moment cloud microphysical scheme. For a better representation of particle shape, size, and number concentration, in this study, the formulation of r_e follows Fu (1996), and the mean axis ratio A_r follows Fu (2007), both based on mean particle size or mass, respectively, for cloud droplets and ice crystals. Details can be found in Gruber et al. (2018).

Consequently, also the optical properties (extinction coefficient, single scattering albedo, and asymmetry factor) of cloud droplets and ice crystals are revised. For ice crystals, the fits are based on a composite of the single scattering parameters extinction efficiency (σ_{EXT}), scattering efficiency (σ_{SCA}), and asymmetry factor (g) obtained from Mie theory, anomalous diffraction theory, geometric optics method, and finite-difference time domain technique covering wavelengths ranging from 0.21 μm to 100 mm (Fu, 1996).

In order to obtain the extinction coefficient (β_{EXT}), the single scattering albedo (ω) and the asymmetry factor (g) for an ensemble of particles from the single particle data, the ice crystal size distribution n, as used for the
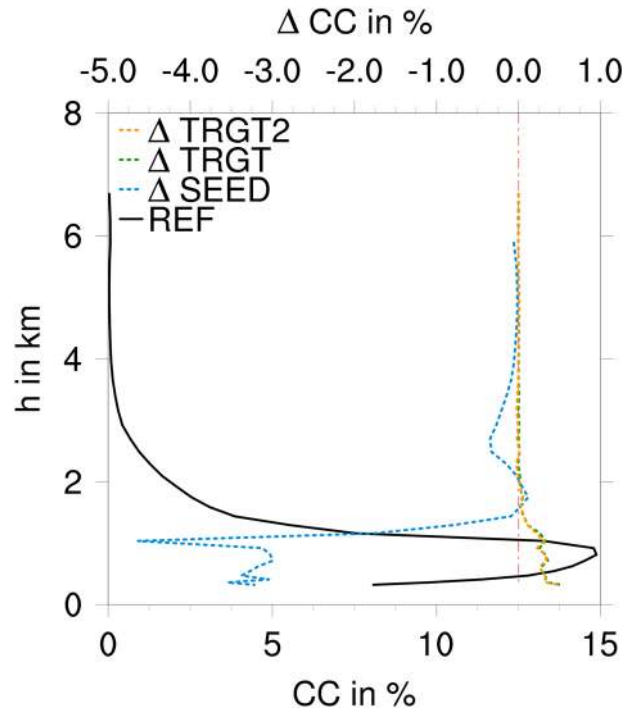
Figure D2. Comparison of liquid (mixed phase) cloud cover averaged over the entire domain and simulation time for reference simulation (black) and seeding strategies *SEED* (blue) and *TRGT* (green). The solid line shows absolute values; dotted lines represent differences compared to the reference simulation. CC = cloud cover.

cloud microphysics, are assumed to follow a generalized Γ function based on the mean hydrometeor size L, with intercept parameter N_0, slope parameter λ, and coefficients ν and μ; detailed explanations and values for the constants can be found in Seifert and Beheng (2006). As for the cloud microphysics, ice crystals are assumed to hexagonal needles

$$n(L) = N_0 L^{\nu} \exp\left(-\lambda L^{\mu}\right) \tag{C1}$$

The spectral optical properties, that is, the extinction coefficient (β_{EXT}), the scattering coefficient (β_{SCA}), the single scattering albedo (ω), and the asymmetry parameter (g) are defined as follows.

$$\beta_{\mathrm{EXT}} = \int_0^{\infty} \sigma_{\mathrm{EXT}}(L)\, n(L)\, \mathrm{d}L \tag{C2}$$

$$\beta_{\mathrm{SCA}} = \int_0^{\infty} \sigma_{\mathrm{SCA}}(L)\, n(L)\, \mathrm{d}L \tag{C3}$$

$$\omega = \frac{\beta_{\mathrm{SCA}}}{\beta_{\mathrm{EXT}}} \tag{C4}$$

$$g = \frac{\int_0^{\infty} g'\sigma_{\mathrm{SCA}}(L)\, n(L)\, \mathrm{d}L}{\int_0^{\infty} \sigma_{\mathrm{SCA}}(L)\, n(L)\, \mathrm{d}L} \quad ; \quad g' = \frac{1}{2}\int_{-1}^{1} \cos\theta P(\cos\theta)\, \mathrm{d}\cos\theta \tag{C5}$$

with scattering angle θ and the scattering phase function P.

First, a particle size distribution (PSD) ensemble containing 7,500 members is defined by systematic variations of the PSD parameters within a wide range. Like this, $\overline{L} = (\nu + 1)/\lambda$ covers a range of $[5, 3000]$ μm; the resulting r_e reaches values up to 300 μm.

For each PSD of this ensemble, the scattering parameters are computed assumed randomly orientation of the ice crystals and spectrally averaged over the wavelength bands of RRTM (Mlawer et al., 1997). Finally,
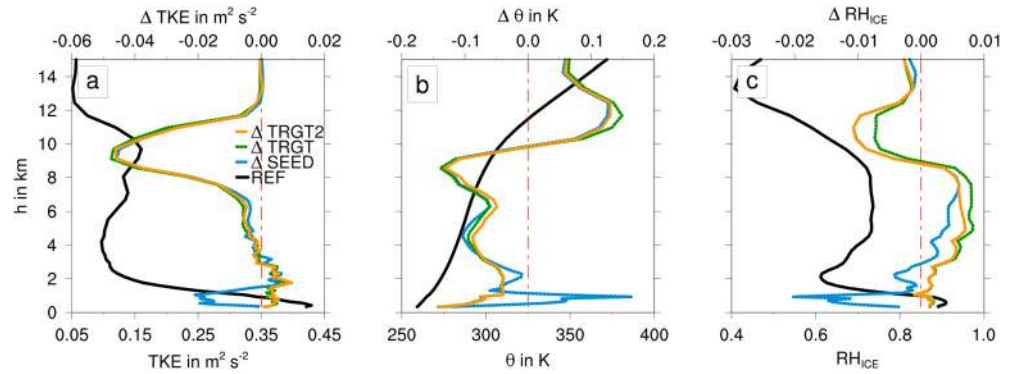
Figure D3. Changes of TKE (a), potential temperature (b), and RH$_{ICE}$ (c) averaged over the entire domain and simulation time for reference simulation (black) and seeding strategies *SEED* (blue), *TRGT* (green), and *TRGT2* (orange). Solid lines are absolute values; dotted lines represent differences compared to the reference simulation. TKE = turbulent kinetic energy.

β_{EXT} and ω are parameterized as function of r_e and g as function of A_r by applying rational, nonlinear ansatz functions (equation (C6)).

$$f(x) = \frac{\displaystyle\sum_{i=0}^{N} a_i x^i}{\displaystyle\sum_{i=0}^{M} b_i x^i} \tag{C6}$$

Likewise, for cloud droplets, data derived from Mie theory (Hu & Stamnes, 1993) is employed.

Appendix D: Idealized Seeding Scenario

Besides two scenarios, where seeding is done either everywhere possible (SEED) or only where necessary to suppress homogeneous nucleation (TRGT), in TRGT2 (see Table 1), the seeding aerosol acts as IN only at high altitudes, that is, with $T < 235$ K. This setup is close to the assumptions made in former studies (e.g., Gasparini et al., 2017; Storelvmo & Herger, 2014).

As in the cirrus regime, temperatures below 235 K are prevailing; the response of cirrus clouds to seeding, that is, a strong suppression of homogeneous nucleation (not shown) resulting in strongly reduced n_{ICE} (Figure D1a) and IWC (Figure D1b), accompanied by a slight increase in r_e (Figure D1c), is found in TRGT2 to an nearly identical extent as in SEED.

At higher temperatures, no nucleation on the seeding aerosol particles is allowed in TRGT2. Therefore, below about 7-km height, the differences between REF and TRGT2 are similar to the results of TRGT. There is a strong decrease in IWC (Figure D1b) and increasing effective radii of ice crystals (Figure D1c). As, except for sparsely sedimenting ice crystals from above, hardly any changes occur concerning the partitioning of liquid and ice in the mixed-phase clouds, glaciation is negligible. In contrast to SEED, CC of both liquid (Figure D2) and frozen clouds (Figure D1d) slightly increases. The reason for this is besides slightly enhanced relative humidity (Figure D3c), especially increased convective activity in TRGT2 (Figure D3a), mainly driven by enhanced cloud top cooling due to the thinned cirrus clouds above (not shown).

Appendix E: Sensitivity to Concentration and Size of Seeding Aerosol and Background Mineral Dust

In this section, additional figures are shown to support the discussion of the impact of changing seeding aerosol properties (Figure E1) in section 4.4, as well as different assumptions concerning the mineral dust background concentrations (Figure E2) on mixed-phase clouds in section 4.5.
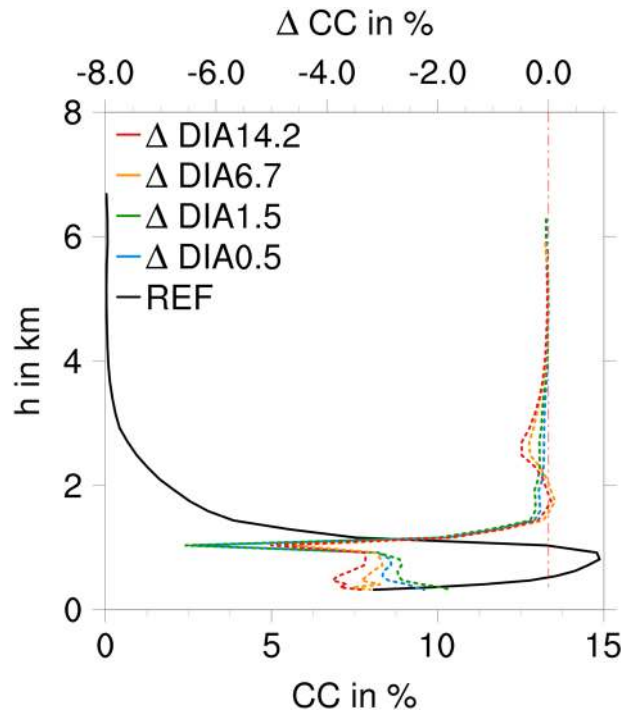
Figure E1. Comparison of liquid (mixed phase) cloud cover averaged over the entire domain and simulation time for reference simulation (black) and simulations with n_{SEED} according to Figure 6 and various d_{SEED} (colors). The solid lines show absolute values; dotted lines represent differences compared to the reference simulation. CC = cloud cover.
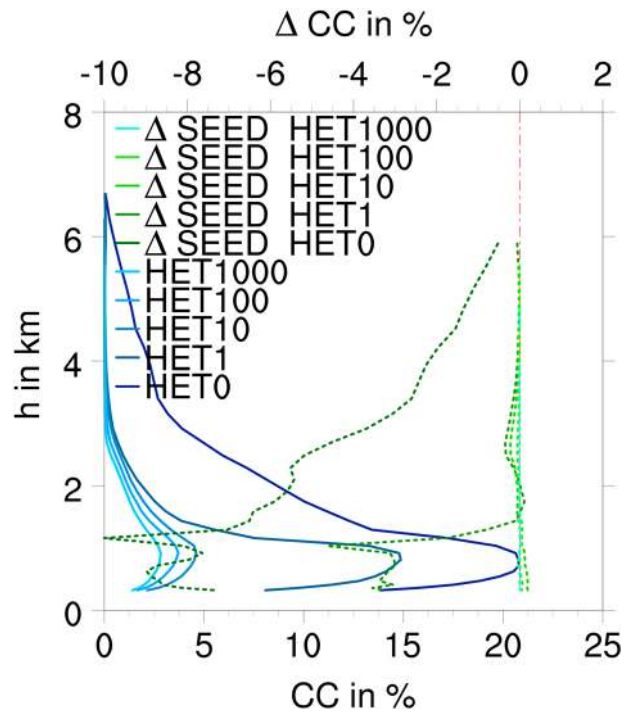

Figure E2. Comparison of liquid (mixed phase) cloud cover for different dust aerosol concentrations averaged over the entire domain and simulation time for reference simulations (blue) and simulations with n_{SEED} according to Figure 6 and d_{SEED} = 6.7 μm. Solid lines are absolute values, dotted lines represent differences compared to the reference simulation. CC = cloud cover.

References

Atkinson, J. D., Murray, B. J., Woodhouse, M. T., Whale, T. F., Baustian, K. J., Carslaw, K. S., et al. (2013). The importance of feldspar for ice nucleation by mineral dust in mixed-phase clouds. *Nature*, *498*, 339–340. https://doi.org/10.1038/nature12278

Baer, F., Arsky, N., Charney, J. J., & Ellingson, R. G. (1996). Intercomparison of heating rates generated by global climate model longwave radiation codes. *Journal of Geophysical Research*, *101*(D21), 26,589–26,603. https://doi.org/10.1029/96JD02511

Bangert, M., Nenes, A., Vogel, B., Vogel, H., Barahona, D., Karydis, V. A., et al. (2012). Saharan dust event impacts on cloud formation and radiation over Western Europe. *Atmospheric Chemistry and Physics*, *12*(9), 4045–4063. https://doi.org/10.5194/acp-12-4045-2012

Barahona, D., Molod, A., & Kalesse, H. (2017). Direct estimation of the global distribution of vertical velocity within cirrus clouds. *Scientific Reports*, *7*, 6840. https://doi.org/10.1038/s41598-017-07038-6

Barahona, D., & Nenes, A. (2009a). Parameterizing the competition between homogeneous and heterogeneous freezing in cirrus cloud formation-monodisperse ice nuclei. *Atmospheric Chemistry and Physics*, *9*(2), 369–381. https://doi.org/10.5194/acp-9-369-2009

Barahona, D., & Nenes, A. (2009b). Parameterizing the competition between homogeneous and heterogeneous freezing in ice cloud formation-polydisperse ice nuclei. *Atmospheric Chemistry and Physics*, *9*(16), 5933–5948. https://doi.org/10.5194/acp-9-5933-2009

Barahona, D., West, R. E. L., Stier, P., Romakkaniemi, S., Kokkola, H., & Nenes, A. (2010). Comprehensively accounting for the effect of giant CCN in cloud activation parameterizations. *Atmospheric Chemistry and Physics*, *10*(5), 2467–2473. https://doi.org/10.5194/acp-10-2467-2010

Binder, H., Boettcher, M., Grams, C. M., Joos, H., Pfahl, S., & Wernli, H. (2017). Exceptional air mass transport and dynamical drivers of an extreme wintertime arctic warm event. *Geophysical Research Letters*, *44*, 12,028–12,036. https://doi.org/10.1002/2017GL075841

Boose, Y., Welti, A., Atkinson, J., Ramelli, F., Danielczok, A., Bingemer, H. G., et al. (2016). Heterogeneous ice nucleation on dust particles sourced from nine deserts worldwide—Part 1: Immersion freezing. *Atmospheric Chemistry and Physics*, *16*(23), 15,075–15,095. https://doi.org/10.5194/acp-16-15075-2016

Caldeira, K., Bala, G., & Cao, L. (2013). The science of geoengineering. *Annual Review of Earth and Planetary Sciences*, *41*(1), 231–256. https://doi.org/10.1146/annurev-earth-042711-105548

Chen, T., Rossow, W. B., & Zhang, Y. (2000). Radiative effects of cloud-type variations. *Journal of Climate*, *13*(1), 264–286. https://doi.org/10.1175/1520-0442(2000)013<0264:REOCTV>2.0.CO;2

Corti, T., & Peter, T. (2009). A simple model for cloud radiative forcing. *Atmospheric Chemistry and Physics*, *9*(15), 5751–5758. https://doi.org/10.5194/acp-9-5751-2009

Crook, J. A., Jackson, L. S., Osprey, S. M., & Forster, P. M. (2015). A comparison of temperature and precipitation responses to different Earth radiation management geoengineering schemes. *Journal of Geophysical Research: Atmospheres*, *120*, 9352–9373. https://doi.org/10.1002/2015JD023269

Crutzen, P. J. (2006). Albedo enhancement by stratospheric sulfur injections: A contribution to resolve a policy Dilemma? *Climatic Change*, *77*(3), 211. https://doi.org/10.1007/s10584-006-9101-y

Cziczo, D. J., Froyd, K. D., Hoose, C., Jensen, E. J., Diao, M., Zondlo, M. A., et al. (2013). Clarifying the dominant sources and mechanisms of cirrus cloud formation. *Science*, *340*(6138), 1320–1324. https://doi.org/10.1126/science.1234145

DeMott, P. J., Cziczo, D. J., Prenni, A. J., Murphy, D. M., Kreidenweis, S. M., Thomson, D. S., et al. (2003). Measurements of the concentration and composition of nuclei for cirrus formation. *Proceedings of the National Academy of Sciences of the United States of America*, *100*(25), 14,655–14,660. https://doi.org/10.1073/pnas.2532677100

DeMott, P. J., Meyers, M. P., & Cotton, W. R. (1994). Parameterization and impact of ice initiation processes relevant to numerical model simulations of cirrus clouds. *Journal of Geophysical Research*, *51*(1), 77–90. https://doi.org/10.1175/1520-0469(1994)051<0077:PAIOII>2.0.CO;2

Eastwood, M. L., Cremel, S., Gehrke, C., Girard, E., & Bertram, A. K. (2008). Ice nucleation on mineral dust particles: Onset conditions, nucleation rates and contact angles. *Journal of Geophysical Research*, *113*, D22203. https://doi.org/10.1029/2008JD010639

Fan, J., Ghan, S., Ovchinnikov, M., Liu, X., Rasch, P. J., & Korolev, A. (2011). Representation of Arctic mixed-phase clouds and the Wegener-Bergeron-Findeisen process in climate models: Perspectives from a cloud-resolving study. *Journal of Geophysical Research*, *116*, D00T07. https://doi.org/10.1029/2010JD015375

Fountoukis, C., & Nenes, A. (2005). Continued development of a cloud droplet formation parameterization for global climate models. *Journal of Geophysical Research*, *110*, D11212. https://doi.org/10.1029/2004JD005591

Friedl-Vallon, F., Gulde, T., Hase, F., Kleinert, A., Kulessa, T., Maucher, G., et al. (2014). Instrument concept of the imaging Fourier transform spectrometer GLORIA. *Atmospheric Measurement Techniques*, *7*(10), 3565–3577. https://doi.org/10.5194/amt-7-3565-2014

Fu, Q. (1996). An accurate parameterization of the solar radiative properties of cirrus clouds for climate models. *Journal of Climate*, *9*(9), 2058–2082. https://doi.org/10.1175/1520-0442(1996)009<2058:AAPOTS>2.0.CO;2

Fu, Q. (2007). A new parameterization of an asymmetry factor of cirrus clouds for climate models. *Journal of the Atmospheric Sciences*, *64*(11), 4140–4150. https://doi.org/10.1175/2007JAS2289.1

Fusina, F., Spichtinger, P., & Lohmann, U. (2007). Impact of ice supersaturated regions and thin cirrus on radiation in the midlatitudes. *Journal of Geophysical Research*, *112*, D24S14. https://doi.org/10.1029/2007JD008449

Futyan, J. M., Russell, J. E., & Harries, J. E. (2005). Determining cloud forcing by cloud type from geostationary satellite data. *Geophysical Research Letters*, *32*, L08807. https://doi.org/10.1029/2004GL022275

Gasch, P., Rieger, D., Walter, C., Khain, P., Levi, Y., Knippertz, P., & Vogel, B. (2017). Revealing the meteorological drivers of the September 2015 severe dust event in the Eastern Mediterranean. *Atmospheric Chemistry and Physics*, *17*(22), 13573–13604. https://doi.org/10.5194/acp-17-13573-2017

Gasparini, B., & Lohmann, U. (2016). Why cirrus cloud seeding cannot substantially cool the planet. *Journal of Geophysical Research: Atmospheres*, *121*, 4877–4893. https://doi.org/10.1002/2015JD024666

Gasparini, B., Münch, S., Poncet, L., Feldmann, M., & Lohmann, U. (2017). Is increasing ice crystal sedimentation velocity in geoengineering simulations a good proxy for cirrus cloud seeding? *Atmospheric Chemistry and Physics*, *17*(7), 4871–4885. https://doi.org/10.5194/acp-17-4871-2017

Gettelman, A., Liu, X., Barahona, D., Lohmann, U., & Chen, C. (2012). Climate impacts of ice nucleation. *Journal of Geophysical Research*, *117*, D20201. https://doi.org/10.1029/2012JD017950

Glantz, P., Bourassa, A., Herber, A., Iversen, T., Karlsson, J., Kirkevåg, A., et al. (2014). Remote sensing of aerosols in the Arctic for an evaluation of global climate model simulations. *Journal of Geophysical Research: Atmospheres*, *119*, 8169–8188. https://doi.org/10.1002/2013JD021279

Gruber, S., Unterstrasser, S., Bechtold, J., Vogel, H., Jung, M., Pak, H., & Vogel, B. (2018). Contrails and their impact on shortwave radiation and photovoltaic power production—A regional model study. *Atmospheric Chemistry and Physics*, *18*(9), 6393–6411. https://doi.org/10.5194/acp-18-6393-2018

Harrington, J. Y., Reisin, T., Cotton, W. R., & Kreidenweis, S. M. (1999). Cloud resolving simulations of Arctic stratus: Part II: Transition-season clouds. *Atmospheric Research*, *51*(1), 45–75. https://doi.org/https://doi.org/10.1016/S0169-8095(98)00098-2

Hartmann, D. L., Ockert-Bell, M. E., & Michelsen, M. L. (1992). The effect of cloud type on earth's energy balance: Global analysis. *Journal of Climate*, *5*(11), 1281–1304. https://doi.org/10.1175/1520-0442(1992)005<1281:TEOCTO>2.0.CO;2

Heinze, R., Dipankar, A., Henken, C. C., Moseley, C., Sourdeval, O., Trömel, S., et al. (2017). Large-eddy simulations over Germany using ICON: A comprehensive evaluation. *Quarterly Journal of the Royal Meteorological Society*, *143*(702), 69–100. https://doi.org/10.1002/qj.2947

Holland, M. M., & Bitz, C. M. (2003). Polar amplification of climate change in coupled models. *Climate Dynamics*, *21*(3), 221–232. https://doi.org/10.1007/s00382-003-0332-6

Hong, Y., Liu, G., & Li, J. L. F. (2016). Assessing the radiative effects of global ice clouds based on cloudsat and CALIPSO Measurements. *Journal of Climate*, *29*(21), 7651–7674. https://doi.org/10.1175/JCLI-D-15-0799.1

Hoose, C., & Möhler, O. (2012). Heterogeneous ice nucleation on atmospheric aerosols: A review of results from laboratory experiments. *Atmospheric Chemistry and Physics*, *12*(20), 9817–9854. https://doi.org/10.5194/acp-12-9817-2012

Hu, Y. X., & Stamnes, K. (1993). An accurate parameterization of the radiative properties of water clouds suitable for use in climate models. *Journal of Climate*, *6*(4), 728–742. https://doi.org/10.1175/1520-0442(1993)006<0728:AAPOTR>2.0.CO;2

Hunt, W. H., Winker, D. M., Vaughan, M. A., Powell, K. A., Lucker, P. L., & Weimer, C. (2009). CALIPSO lidar description and performance assessment. *Journal of Atmospheric and Oceanic Technology*, *26*(7), 1214–1228. https://doi.org/10.1175/2009JTECHA1223.1

Ickes, L., Welti, A., Hoose, C., & Lohmann, U. (2015). Classical nucleation theory of homogeneous freezing of water: Thermodynamic and kinetic parameters. *Physical Chemistry Chemical Physics*, *17*, 5514–5537. https://doi.org/10.1039/C4CP04184D

Jackson, L. S., Crook, J. A., & Forster, P. M. (2016). An intensified hydrological cycle in the simulation of geoengineering by cirrus cloud thinning using ice crystal fall speed changes. *Journal of Geophysical Research: Atmospheres*, *121*, 6822–6840. https://doi.org/10.1002/2015JD024304

Jensen, E., Diskin, G., Lawson, R. P., Lance, S., Bui, T. P., Hlavka, D., et al. (2013). Ice nucleation and dehydration in the tropical tropopause layer. *Proceedings of the National Academy of Sciences of the United States of America*, *110*(6), 2041–2046. https://doi.org/10.1073/pnas.1217104110

Jensen, E., Ueyama, R., Pfister, L., Bui, T. V., Alexander, M. J., Podglajen, A., et al. (2016). High-frequency gravity waves and homogeneous ice nucleation in tropical tropopause layer cirrus. *Geophysical Research Letters*, *43*, 6629–6635. https://doi.org/10.1002/2016GL069426

Johansson, S., Woiwode, W., Höpfner, M., Friedl-Vallon, F., Kleinert, A., Kretschmer, E., et al. (2018). Airborne limb-imaging measurements of temperature, HNO_3, O_3, $ClONO_2$, H_2O and CFC-12 during the Arctic winter 2015/16: Characterization, in-situ validation and comparison to Aura/MLS. *Atmospheric Measurement Techniques Discussions*, *2018*, 1–31. https://doi.org/10.5194/amt-2018-52

Joos, H., Spichtinger, P., Reutter, P., & Fusina, F. (2014). Influence of heterogeneous freezing on the microphysical and radiative properties of orographic cirrus clouds. *Atmospheric Chemistry and Physics*, *14*(13), 6835–6852. https://doi.org/10.5194/acp-14-6835-2014

Kärcher, B., Hendricks, J., & Lohmann, U. (2006). Physically based parameterization of cirrus cloud formation for use in global atmospheric models. *Journal of Geophysical Research*, *111*, D01205. https://doi.org/10.1029/2005JD006219

Kärcher, B., & Lohmann, U. (2002). A parameterization of cirrus cloud formation: Homogeneous freezing of supercooled aerosols. *Journal of Geophysical Research*, *107*(D2), AAC 4–1–AAC 4-10. https://doi.org/10.1029/2001JD000470

Kärcher, B., & Lohmann, U. (2003). A parameterization of cirrus cloud formation: Heterogeneous freezing. *Journal of Geophysical Research*, *108*(D14), 4402. https://doi.org/10.1029/2002JD003220

Kärcher, B., & Ström, J. (2003). The roles of dynamical variability and aerosols in cirrus cloud formation. *Atmospheric Chemistry and Physics*, *3*(3), 823–838. https://doi.org/10.5194/acp-3-823-2003

Khosrawi, F., Kirner, O., Sinnhuber, B. M., Johansson, S., Höpfner, M., Santee, M. L., et al. (2017). Denitrification, dehydration and ozone loss during the 2015/2016 Arctic winter. *Atmospheric Chemistry and Physics*, *17*(21), 12893–12910. https://doi.org/10.5194/acp-17-12893-2017

Kienast-Sjögren, E., Rolf, C., Seifert, P., Krieger, U. K., Luo, B. P., Krämer, M., & Peter, T. (2016). Climatological and radiative properties of midlatitude cirrus clouds derived by automatic evaluation of lidar measurements. *Atmospheric Chemistry and Physics*, *16*(12), 7605–7621. https://doi.org/10.5194/acp-16-7605-2016

Kiselev, A., Bachmann, F., Pedevilla, P., Cox, S. J., Michaelides, A., Gerthsen, D., & Leisner, T. (2017). Active sites in heterogeneous ice nucleation—The example of K-rich feldspars. *Science*, *355*(6323), 367–371. https://doi.org/10.1126/science.aai8034

Köhler, C. G., & Seifert, A. (2015). Identifying sensitivities for cirrus modelling using a two-moment two-mode bulk microphysics scheme. *Tellus*, *67*(1), 24494. https://doi.org/10.3402/tellusb.v67.24494

Koop, T., Luo, B., Tsias, A., & Peter, T. (2000). Water activity as the determinant for homogeneous ice nucleation in aqueous solutions. *Nature*, *406*, 611–614. https://doi.org/10.1038/s41598-017-07038-6

Krämer, M., Rolf, C., Luebke, A., Afchine, A., Spelten, N., Costa, A., et al. (2016). A microphysics guide to cirrus clouds—Part 1: Cirrus types. *Atmospheric Chemistry and Physics*, *16*(5), 3463–3483. https://doi.org/10.5194/acp-16-3463-2016

Krämer, M., Schiller, C., Afchine, A., Bauer, R., Gensch, I., Mangold, A., et al. (2009). Ice supersaturations and cirrus cloud crystal numbers. *Atmospheric Chemistry and Physics*, *9*(11), 3505–3522. https://doi.org/10.5194/acp-9-3505-2009

Kuebbeler, M., Lohmann, U., Hendricks, J., & Kärcher, B. (2014). Dust ice nuclei effects on cirrus clouds. *Atmospheric Chemistry and Physics*, *14*(6), 3027–3046. https://doi.org/10.5194/acp-14-3027-2014

Kumar, P., Sokolik, I. N., & Nenes, A. (2009). Parameterization of cloud droplet formation for global and regional models: Including adsorption activation from insoluble CCN. *Atmospheric Chemistry and Physics*, *9*(7), 2517–2532. https://doi.org/10.5194/acp-9-2517-2009

Lamquin, N., Stubenrauch, C. J., Gierens, K., Burkhardt, U., & Smit, H. (2012). A global climatology of upper-tropospheric ice supersaturation occurrence inferred from the Atmospheric Infrared Sounder calibrated by MOZAIC. *Atmospheric Chemistry and Physics*, *12*(1), 381–405. https://doi.org/10.5194/acp-12-381-2012

Latham, J. (1990). Control of global warming? *Nature*, *347*, 339–340. https://doi.org/10.1038/347339b0

Latham, J. (2002). Amelioration of global warming by controlled enhancement of the albedo and longevity of low-level maritime clouds. *Atmospheric Science Letters*, *3*(2-4), 52–58. https://doi.org/10.1006/asle.2002.0099

Lohmann, U., & Gasparini, B. (2017). A cirrus cloud climate dial? *Science*, *357*(6348), 248–249. https://doi.org/10.1126/science.aan3325

Lohmann, U., McFarlane, N., Levkov, L., Abdella, K., & Albers, F. (1999). Comparing different cloud schemes of a single column model by using mesoscale forcing and nudging technique. *Journal of Climate*, *12*(2), 438–461. https://doi.org/10.1175/1520-0442(1999)012<0438:CDCSOA>2.0.CO;2

Lohmann, U., Spichtinger, P., Jess, S., Peter, T., & Smit, H. (2008). Cirrus cloud formation and ice supersaturated regions in a global climate model. *Environmental Research*, *3*(4), 045022. https://doi.org/10.1088/1748-9326/3/4/045022

Lundgren, K., Vogel, B., Vogel, H., & Kottmeier, C. (2013). Direct radiative effects of sea salt for the Mediterranean region under conditions of low to moderate wind speeds. *Journal of Geophysical Research: Atmospheres*, *118*, 1906–1923. https://doi.org/10.1029/2012JD018629

Matus, A. V., & L'Ecuyer, T. S. (2017). The role of cloud phase in Earth's radiation budget. *Journal of Geophysical Research: Atmospheres*, *122*, 2559–2578. https://doi.org/10.1002/2016JD025951

McFarlane, S. A., Mather, J. H., & Ackerman, T. P. (2007). Analysis of tropical radiative heating profiles: A comparison of models and observations. *Journal of Geophysical Research*, *112*, D14218. https://doi.org/10.1029/2006JD008290

Mitchell, D., & Finnegan, W. (2009). Modification of cirrus clouds to reduce global warming. *Environmental Research*, *4*(4), 045102. https://doi.org/10.1088/1748-9326/4/4/045102

Mitchell, D., Mishra, S., & Paul Lawson, R. (2011). Planet Earth 2011—Global warming challenges and opportunities for policy and practice. In E. G. Caravannis (Ed.) (vol. 12, pp. 257–288). Rijeka, Croatia: InTech. https://doi.org/10.5772/902

Mlawer, E. J., Taubman, S. J., Brown, P. D., Iacono, M. J., & Clough, S. A. (1997). Radiative transfer for inhomogeneous atmospheres: RRTM, a validated correlated-k model for the longwave. *Journal of Geophysical Research*, *102*(D14), 16663–16682. https://doi.org/10.1029/97JD00237

Morrison, H., de Boer, G., Feingold, G., Harrington, J., Shupe, M. D., & Sulia, K. (2012). Resilience of persistent Arctic mixed-phase clouds. *Nature*, *5*, 11–17. https://doi.org/10.1038/ngeo1332

Muri, H., Kristjánsson, J. E., Storelvmo, T., & Pfeffer, M. A. (2014). The climatic effects of modifying cirrus clouds in a climate engineering framework. *Journal of Geophysical Research: Atmosphere*, *119*, 4174–4191. https://doi.org/10.1002/2013JD021063

Myhre, G., Shindell, D., Bréon, F.-M., Collins, W., Fuglestvedt, J., Huang, J., et al. (2013). Anthropogenic and natural radiative forcing. In T. F. Stocker, D. Qin, G.-K. Plattner, M. Tignor, S. K. Allen & J. Boschung (Eds.), *Climate Change 2013: The Physical Science Basis. Contribution of Working Group I to the Fifth Assessment Report of the Intergovernmental Panel on Climate Change* (pp. 659–740). Cambridge, UK: Cambridge University Press.

Niemand, M., Möhler, O., Vogel, B., Vogel, H., Hoose, C., Connolly, P., et al. (2012). A particle-surface-area-based parameterization of immersion freezing on desert dust particles. *Journal of the Atmospheric Sciences*, *69*(10), 3077–3092. https://doi.org/10.1175/JAS-D-11-0249.1

Penner, J. E., Zhou, C., & Liu, X. (2015). Can cirrus cloud seeding be used for geoengineering? *Geophysical Research Letters*, *42*, 8775–8782. https://doi.org/10.1002/2015GL065992

Phillips, V. T. J., DeMott, P. J., & Andronache, C. (2008). An empirical parameterization of heterogeneous ice nucleation for multiple chemical species of aerosol. *Journal of the Atmospheric Sciences*, *65*(9), 2757–2783. https://doi.org/10.1175/2007JAS2546.1

Phillips, V. T. J., Demott, P. J., Andronache, C., Pratt, K. A., Prather, K. A., Subramanian, R., & Twohy, C. (2013). Improvements to an empirical parameterization of heterogeneous ice nucleation and its comparison with observations. *Journal of the Atmospheric Sciences*, *70*(2), 378–409. https://doi.org/10.1175/JAS-D-12-080.1

Powell, K. A., Hostetler, C. A., Vaughan, M. A., Lee, K. P., Trepte, C. R., Rogers, R. R., et al. (2009). CALIPSO Lidar calibration algorithms. Part I: Nighttime 532-nm parallel channel and 532-nm perpendicular channel. *Journal of Atmospheric and Oceanic Technology*, *26*(10), 2015–2033. https://doi.org/10.1175/2009JTECHA1242.1

Pruppacher, H. R., & Klett, J. D. (1997). *Microphysics of clouds and precipitation*. Dordrecht: Kluwer Academic Publishers.

Rauscher, S. A., O'Brien, T. A., Piani, C., Coppola, E., Giorgi, F., Collins, W. D., & Lawston, P. M. (2016). A multimodel intercomparison of resolution effects on precipitation: Simulations and theory. *Climate Dynamics*, *47*(7), 2205–2218. https://doi.org/10.1007/s00382-015-2959-5

Rieger, D., Bangert, M., Bischoff-Gauss, I., Förstner, J., Lundgren, K., Reinert, D., et al. (2015). ICON-ART 1.0—A new online-coupled model system from the global to regional scale. *Geoscientific Model Development*, *8*(6), 1659–1676. https://doi.org/10.5194/gmd-8-1659-2015

Rieger, D., Steiner, A., Bachmann, V., Gasch, P., Förstner, J., Deetz, K., et al. (2017). Impact of the 4 April 2014 Saharan dust outbreak on the photovoltaic power generation in Germany. *Atmospheric Chemistry and Physics*, *17*(21), 13391–13415. https://doi.org/10.5194/acp-17-13391-2017

Riese, M., Oelhaf, H., Preusse, P., Blank, J., Ern, M., Friedl-Vallon, F., et al. (2014). Gimballed Limb Observer for Radiance Imaging of the Atmosphere (GLORIA) scientific objectives. *Atmospheric Measurement Techniques*, *7*(7), 1915–1928. https://doi.org/10.5194/amt-7-1915-2014

Rossow, W. B., & Schiffer, R. A. (1999). Advances in understanding clouds from ISCCP. *Bulletin of the American Meteorological Society*, *80*(11), 2261–2288. https://doi.org/10.1175/1520-0477(1999)080<2261:AIUCFI>2.0.CO;2

Sassen, K., Wang, Z., & Liu, D. (2008). Global distribution of cirrus clouds from CloudSat/Cloud-Aerosol Lidar and Infrared Pathfinder Satellite Observations (CALIPSO) measurements. *Journal of Geophysical Research*, *113*, D00A12. https://doi.org/10.1029/2008JD009972

Schmidt, C. T., & Garrett, T. J. (2013). A simple framework for the dynamic response of cirrus clouds to local diabatic radiative heating. *Journal of the Atmospheric Sciences*, *70*(5), 1409–1422. https://doi.org/10.1175/JAS-D-12-056.1

Seifert, A., & Beheng, K. D. (2006). A two-moment cloud microphysics parameterization for mixed-phase clouds. Part 1: Model description. *Meteorology and Atmospheric Physics*, *92*(1), 45–66. https://doi.org/10.1007/s00703-005-0112-4

Spang, R., Remedios, J., & Barkley, M. (2004). Colour indices for the detection and differentiation of cloud types in infra-red limb emission spectra. *Advances in Space Research*, *33*(7), 1041–1047. https://doi.org/10.1016/S0273-1177(03)00585-4

Spichtinger, P., Gierens, K., & Read, W. (2003). The global distribution of ice-supersaturated regions as seen by the Microwave Limb Sounder. *Quarterly Journal of the Royal Meteorological Society*, *129*(595), 3391–3410. https://doi.org/10.1256/qj.02.141

Spichtinger, P., Gierens, K., Smit, H. G. J., Ovarlez, J., & Gayet, J. F. (2004). On the distribution of relative humidity in cirrus clouds. *Atmospheric Chemistry and Physics*, *4*(3), 639–647. https://doi.org/10.5194/acp-4-639-2004

Stephens, G. L., Vane, D. G., Boain, R. J., Mace, G. G., Sassen, K., Wang, Z., et al. the CloudSat Science Team (2002). The CloudSat mission and the A-Train: A new dimension of space-based observations of clouds and precipitation. *Bulletin of the American Meteorological Society*, *83*(12), 1771–1790. https://doi.org/10.1175/BAMS-83-12-1771

Stevens, B., Giorgetta, M., Esch, M., Mauritsen, T., Crueger, T., Rast, S., et al. (2013). Atmospheric component of the MPI-M Earth System Model: ECHAM6. *Journal of Advances in Modeling Earth Systems*, *5*, 146–172. https://doi.org/10.1002/jame.20015

Storelvmo, T., Boos, W. R., & Herger, N. (2014). Cirrus cloud seeding: A climate engineering mechanism with reduced side\ref{} effects? *Philosophical Transactions of the Royal Society*, *372*(2031), 20140116. https://doi.org/10.1098/rsta.2014.0116

Storelvmo, T., & Herger, N. (2014). Cirrus cloud susceptibility to the injection of ice nuclei in the upper troposphere. *Journal of Geophysical Research: Atmospheres*, *119*, 2375–2389. https://doi.org/10.1002/2013JD020816

Storelvmo, T., Kristjansson, J. E., Muri, H., Pfeffer, M., Barahona, D., & Nenes, A. (2013). Cirrus cloud seeding has potential to cool climate. *Geophysical Research Letters*, *40*, 178–182. https://doi.org/10.1029/2012GL054201

Verlinde, J., Rambukkange, M. P., Clothiaux, E. E., McFarquhar, G. M., & Eloranta, E. W. (2013). Arctic multilayered, mixed-phase cloud processes revealed in millimeter-wave cloud radar Doppler spectra. *Journal of Geophysical Research: Atmospheres*, *113*, 199–213. https://doi.org/10.1002/2013JD020183

Wild, M., Folini, D., Hakuba, M. Z., Schär, C., Seneviratne, S. I., Kato, S., et al. (2015). The energy balance over land and oceans: An assessment based on direct observations and CMIP5 climate models. *Climate Dynamics*, *44*(11), 3393–3429. https://doi.org/10.1007/s00382-014-2430-z

Winker, D. M., Hunt, W. H., & McGill, M. J. (2007). Initial performance assessment of CALIOP. *Geophysical Research Letters*, *34*, L19803. https://doi.org/10.1029/2007GL030135

Winker, D. M., Vaughan, M. A., Omar, A., Hu, Y., Powell, K. A., Liu, Z., et al. (2009). Overview of the CALIPSO mission and CALIOP data processing algorithms. *Journal of Atmospheric and Oceanic Technology*, *26*(11), 2310–2323. https://doi.org/10.1175/2009JTECHA1281.1

Xie, Y., Li, Z., Li, L., Wagener, R., Abboud, I., Li, K., et al. (2018). Aerosol optical, microphysical, chemical and radiative properties of high aerosol load cases over the Arctic based on AERONET measurements. *Nature*, *8*(9376), 823–838. https://doi.org/10.1038/s41598-018-27744-z

Zängl, G., Reinert, D., Rípodas, P., & Baldauf, M. (2015). The ICON (ICOsahedral Non-hydrostatic) modelling framework of DWD and MPI-M: Description of the non-hydrostatic dynamical core. *Quarterly Journal of the Royal Meteorological Society*, *141*(687), 563–579. https://doi.org/10.1002/qj.2378